

The Canadian Journal of Chemical Engineering (CJCE)

<https://onlinelibrary.wiley.com/journal/1939019x>

ACCEPTED FRIDAY APRIL 5TH, 2024.

NUMERICAL SIMULATION OF NATURAL CONVECTION IN A RECTANGULAR ENCLOSURE FILLED WITH POROUS MEDIUM SATURATED WITH MAGNETIC NANOFLUID USING BUONGIORNO'S TWO-COMPONENT MODEL

K Venkatadri*

*Department of Mathematics, Indian Institute of Information Technology Sri City, Tirupati-517464, A.P., India. *Corresponding author- Email: venkatadri.venki@gmail.com and venkatadri.k@iiits.in*

K. V. Narasimha Murthy

Dept. of Mathematics, Madanapalle Institute of Technology & Science, Madanapalle, 517325, A.P., India. Email murthy.koundinyas@gmail.com

Tasveer A. Bég

Engineering Mechanics Research, Israfil House, Dickenson Road, Manchester, M13, UK.

Email: tasveerabeg@gmail.com

O. Anwar Bég and Sireetorn Kuharat

Multi-Physical Engineering Sciences Group, Aeronautical/Mechanical Engineering, Salford University, Corrosion/Coatings Lab, 3-08, SEE Building, Manchester, M54WT, UK.

Emails: O.A.Beg@salford.ac.uk; S.Kuharat2@salford.ac.uk

ABSTRACT

Motivated by studying emerging nanofluid-based magnetic fuel cells and hybrid direct absorber solar collectors, a numerical study is presented for buoyancy-driven flow in a vertical enclosure containing a porous medium saturated with magnetised nanofluid flow under a transverse static magnetic field. The enclosure features adiabatic side walls and vertical heat slits, ensuring consistent cold temperatures on the lower and upper bounded walls. The side walls of the regime are insulated, and the hot slits are centrally located on these walls. The finite difference method (FDM) is applied to employ the transformed dimensionless vorticity-stream function (VSF) formulation of the transport equations. The impact of pertinent parameters on isotherm, streamline, iso-concentration, average Nusselt and Sherwood numbers are visualized with contour plots and graphs. Increasing Darcy number values tend to amplify the isotherm magnitudes. Higher Hartmann (magnetic) number values, on the other hand, lead to a reduction in local Nusselt number profiles but do not significantly modify the local Sherwood number. The porous medium permeability, as simulated via the Darcy number, has a strong impact on streamlines, thermal contours, and iso-concentrations. A reduction in Darcy's number suppresses local Nusselt and Sherwood numbers, whereas an elevation in

Rayleigh's number enhances them. Increasing the Buongiorno nanoscale Brownian motion parameter enhances local Nusselt and Sherwood numbers at both cold walls of the enclosure. The simulations provide a deeper insight into enclosure flows involving electrically conducting nanofluids in advanced processing systems for nanomaterials and hybrid fuel cells utilizing electromagnetic and liquid fuel technologies.

KEYWORDS: *Buongiorno two-component nanofluid mixture model, rectangular enclosure, laminar flow, magnetized nanofluid, porous medium, Finite difference method; Sherwood number; Nusselt number; vortex cells; electromagnetic fuel cells.*

1. INTRODUCTION

Nanofluids which are characterized as colloidal suspensions and synthesized via nanoparticles dispersed within a base fluid, have garnered significant attention across various technological fields due to their unique and enhanced properties, such as improved heat transfer in electronics, solar collectors, fuel cells and cooling systems. By nanoparticle addition to the base fluid, nanofluids have shown a significant improvement in thermal performance relative to traditional fluids. One of the well-known models for modelling nanofluid hydrothermal characteristics is Buongiorno's [1] two-component nanoscale model which includes both conservation of energy and nanoparticle diffusion (mass transfer) equations. This formulation has been very successfully applied for investigating enhanced heat transfer in nanofluids and emphasizes thermophoresis and random diffusion (Brownian motion) as the dominant mechanisms. Several researchers have conducted investigations on buoyancy-driven convective flow in a closed regime filled with Buongiorno nanofluids to explore the heat transfer performance in various geometrical shapes using a wide range of computational techniques. Bouafia *et al.* [2] deployed a Galerkin finite element method to obtain the steady-state convective flow in a porous square cavity filled by nano liquid with two isothermal cylindrical sources. They noted that convection heat transfer (both mean and local thermal transport rate) is boosted with a growth in Rayleigh and permeability, volume fraction of nanoparticles, but is reduced with dimensionless wall thickness. In their study, Natesan *et al.* [3] harnessed the power of a control volume SIMPLE algorithm to simulate the intricate interplay of thermo-solutal natural convection within a square enclosure. The enclosure was filled with a nanofluid comprised of alumina water, and the simulation aimed to unravel the complex dynamics inherent in such systems, noting that nanoparticle effectiveness is optimized when thermal and species thermal forces are equal but oppose each other. Motlagh *et al.* [4] employed a control volume method to rigorously examine the intricacies of free convection

thermal transport within an oblique enclosure permeated with a porous medium. This medium was saturated with two distinct nanofluids— $\text{Al}_2\text{O}_3/\text{water}$ and Cu/water —thus contributing to a comprehensive exploration of the phenomenon. They noted that medium permeability exerts a significant effect on Nusselt numbers and internal thermal distributions and is optimized at large values of the porous Rayleigh number. They also found that copper nanoparticles achieve a more homogenous streamline and isotherm distribution relative to alumina nanoparticles. Yu *et al.* [5] used wavelet-homotopy computational technique to investigate the mixed convection of laminar flow in a tilted lid-driven enclosure. They considered the upper and lower walls to be thermally insulated and the two side walls to be sinusoidally heated. Sheremet *et al.* [6] used a FDM on non-uniform mesh and successive under relaxation methods to compute the thermal flow in a porous enclosure filled with a nanofluid, exhibiting three-dimensional characteristics. They demonstrated that when dealing with low quantities, the outcome is different Ra and Le numbers and with strong thermophoresis, there is an uneven distribution of nanoparticles inside the enclosure. Oztop and Abu-Nada [7] employed a finite volume algorithm and the Maxwell-Garnetts nanoscale model to simulate convection phenomena in rectangular enclosures with partial heating, where nanofluids are present, exhibiting natural heat transfer consisting of copper, titania, and alumina in water. The results they obtained showed that the average Nusselt number rise for all the Rayleigh number values as the volume fraction of the three nanoparticles rose. Notably, they observed a more pronounced internal circulation for alumina nanoparticles compared to titania nanoparticles at lower Rayleigh number values. In a separate study, Garoosi *et al.* [8] studied the heat transport characteristics of water based Al_2O_3 nanofluid under conjugate convection conditions within a square cavity subjected to lateral heating. Concurrently, Sheremet *et al.* [9] explored a comprehensive numerical analysis to explore the free convection behavior of nanofluid in two interconnected triangular chambers, incorporating the influences of Brownian motion and thermophoresis. They observed that in contrast to the upper cavity, the second triangular cavity exhibited greater sensitivity to variations in both buoyancy number and buoyancy-ratio factors. Sheremet *et al.* [10] delved deeper into examining how sinusoidal thermal distributions along the side walls influence buoyancy flow within a wavy porous cavity in presence of nanofluid. Their study employed Buongiorno's mathematical model to enhance our understanding of the associated effects. Cimpean and Pop [11] implemented a central difference scheme with Gauss-Siedel iteration to simulate the thermal flow of nanofluid in a tilted square porous enclosure using Buongiorno's mathematical model. These investigations have confirmed the excellent capability of two-component nanoscale model in accurately

evaluating key characteristics of nanofluids in porous cavities, in the presence of a range of complex effects including wavy boundary surfaces and non-uniform heating.

Natural convection is a phenomenon that occurs when there is a thermal gradient within a fluid, resulting in the movement of the fluid due to buoyancy forces. It is an important mode of heat transfer in various engineering applications including fuel cells, enclosure materials processing and direct absorber solar collectors. Studies have investigated various aspects of nanofluid flow in different types of enclosures, such as square/rectangular cavities, cavities with obstacles, wavy enclosures, and trapezoidal/circular/annular cavities [12]. The behavior of nanofluids in enclosures has been explored in the context of natural convection, free convection and also mixed convection, considering factors such as the porous media, heat sources and geometric parameters of heaters [13-16]. Furthermore, how the heat transfer rates are influenced by the properties of nanofluids, including viscosity and dynamic thermal conductivity within the enclosures has been a key focus of investigation [17]. The help of nanofluids in different flow regimes, such as laminar flow, and their impacts on the thermal performance of systems, such as automobile cooling systems, has also been studied Yasuri & Soleimani [18]. Additionally, the application of nanofluidic channels with Janus nano building blocks for electrokinetic energy conversion has been explored, highlighting the potential for innovative energy conversion technologies [19]. Moreover, the exploration of nanofluidic analytical devices has garnered attention for the development of innovative features and applications, highlighting the diverse range of potential uses for nanofluid flow within enclosures [20].

An important subset of nano-liquids is *electromagnetic nanofluids* [21]. These feature magnetic nanoparticles suspended in electrically conducting base fluids and enable magnetohydrodynamic (MHD) effects. Magnetic nanofluids have further functionalities which are not available in conventional nanofluids. They permit manipulation of heat, mass and momentum characteristics with the applied external magnetic field which may be static or alternating in nature. This non-intrusive technology has great potential in next generation magnetic fuel cells [22] where both nanofluids and hydromagnetic can be combined to optimize performance. Many excellent studies of magnetic nanofluid synthesis have been communicated where electrical conductivity, viscosity and thermal capacity for different nanoparticles and base fluids have been explored in a range of fuel cell applications including PEM fuel cells, zinc oxide-insulated oil electro-conductive nanofluid batteries, nanoparticle/nanotube-enhanced ionic magnetic capacitors, magnetohydrodynamic microbial nano-liquid fuel cells etc [23-32]. Excellent physico-mathematical aspects of MHD have been elucidated by Rathore

and Panwar [33] and Xiros [34] for emerging electromagnetic fuel cell applications covering many complex aspects including thermos-acoustics, plasma, resonance, durability, efficiency and different working fluids. Magnetic nanofluids have also attracted considerable attention in a number of other areas. Noteworthy disciplines in this regard include magnetic thermal duct processing in nuclear reactors [36], smart tribology in locomotive and aerospace contact mechanics [37], packaging and coating applications [38]- [40], spin coating of ferromagnetic nano-polymers [41, 42]. Additionally, state of the art biomedical treatments [43] which include magnetic hyperthermia-based cancer therapy, temperature, defect detection, pH, cation sensors, tunable optical filters, dynamic seals and other technologies are exploiting optical, thermal, magnetic and rheological properties of a huge range of magnetic nanofluids. With regard to the focus of the present work, namely magnetic nanofluid-based enclosures for fuel cells, considerable activity has emerged in computational simulations in the past decade or so. Roy *et al.* [44] utilized a finite difference code to analyse the magnetized hybrid copper-alumina-water nanofluid convection in multiple heat sources of the enclosure under the action of an inclined static Lorenz force. He showed that vortex strength of circulating cells in the domain is increased with Rayleigh number but reduced with magnetic field parameter. He also showed that with more heat sources, greater magnetic field inclination (which alters the Lorentzian magnetic body force components) and Rayleigh number, thermal transfer to the boundaries (average Nusselt number) is elevated. Al-Kouz *et al.* [45] employed the Galerkin FEM through the utilization of the COMSOL Multiphysics to compute the production of entropy as a result of natural circulation in magnetized $\text{Fe}_3\text{O}_4/\text{CNT}$ -water hybrid nanofluid in a wavy-walled dual compartment (porous/purely fluid) trapezoidal enclosure. They observed that a stronger magnetic field and thermal buoyancy force suppress the average Bejan number (entropy generation rate). In contrast, the lower permeability of the porous zone (Darcy number) enhances the heat transfer rate when the Rayleigh number reaches high values by up to 20%. Azizul *et al.* [46] applied a Galerkin weighted residual and FEM to simulate the two-dimensional configuration, a rectangular cavity containing a magnetic alumina nanofluid and having wavy walls is subjected to mixed convection. containing triple fins. When a great magnetic field is combined with a high-volume fraction of nanoparticles, it was discovered that the rate of heat transfer is increased. Further works include Sumithra *et al.* [47] (who studied the influence of hot slits and inclined magnetic field on Buongiorno magnetic nanofluids in a rectangular porous media enclosure with thermally insulated walls with the Keller box implicit FDM) and Thirumalaisamy *et al.* [48] (who computed the effects of Ohmic magnetic heating and heat generation and absorption on the relative performance of magnetized $\gamma\text{Al}_2\text{O}_3$ and γ -

$\text{Al}_2\text{O}_3\text{-C}_2\text{H}_6\text{O}_2$ in square enclosure filled with saturated porous material containing nanofluids with electroconductive properties). These investigations all confirmed the excellent functionality of magnetic nanofluids in further achieving better regulation of thermal characteristics compared with conventional electrically non-conducting nanofluids.

An examination of existing literature indicates that the thermo-solutal convection in saturated porous medium is enclosed within a rectangle enclosure with a Newtonian two-component electromagnetic Buongiorno nanofluid, and featuring adiabatic horizontal walls and vertical hot slits, has been minimally explored. Specifically, there is limited focus on scenarios where uniform cold temperatures are sustained at both the lower and upper walls. This motivation for the present investigation which has applications in simulating hybrid magnetic nanofluid-based fuel cells, solar collectors and other systems such as materials batch processing with electro-conductive nanofluids. Buongiorno's model is deployed. The vertical walls of the enclosure are adiabatic, and hot slits are positioned at the centre of these walls. The vorticity-stream function formulation is utilized in which the vorticity is directly related to the rotation of fluid elements, and the stream function provides a natural representation of flow patterns. The FDM is utilized to address the equations that govern the conservation of mass, momentum, energy, and the concentration of nanoparticles (species) in their transformed dimensionless VSF form, taking into account appropriate wall conditions. Streamline, isotherm, and iso-concentration, average Nusselt and average Sherwood numbers are affected by important parameters and are visualized with contour plots and graphs. Validation of the FDM solutions with previous studies is included. *The novelties of the present study are the simultaneous consideration of a physically realistic range of magnetic field, porous medium, thermal buoyancy and nanoscale parameter values and extensive visualization of the internal thermal fluid characteristics and wall gradient characteristics (Nusselt and Sherwood number). An optimized MAC algorithm is deployed for the numerical solution with extensive validation. Furthermore, a very deep physical interpretation of results is provided compared with previous studies and the implications for hybrid nano-magnetic fuel cells and solar collectors are more rigorously appraised.*

2. MATHEMATICAL FORMULATION

In this current study, the focus is on the motion of fluids due to temperature differences, occurring inside a rectangular container containing a homogenous, non-tortuous, isotropic, a medium that allows the passage of fluids and is filled with a nanofluid that conducts electricity and cannot be compressed under transverse magnetic field is examined theoretically and

computationally. The model is a 2-dimensional representation of a hybrid magnetic fuel cell. The computational domain is illustrated in **Figure 1**, depicting the Cartesian coordinate system where x and y represent the horizontal and vertical coordinates, and L denotes the width of the enclosure with $2L$ denoting the height (i. e. aspect ratio is 2). The enclosure features thermally insulated vertical walls, with hot slits located at the centres of these walls. Additionally, horizontal walls are maintained as isothermal cold walls. The boundaries are electrically insulated. Since the flow is laminar (low Reynolds number), viscous effects hold more prominence than inertial effects. As a result, we deploy the Darcy drag force model for bulk porous media impedance. To examine the density fluctuation within the cavity, the Oberbeck-Boussinesq approximation is employed, while the remaining physical properties are assumed to be constant. The porous medium is isotropic i. e. permeability is equal in both the x and y directions. Hall current, magnetic induction, Ohmic dissipation (Joule heating) and Maxwell displacement current effects are ignored as is thermal and solutal stratification.

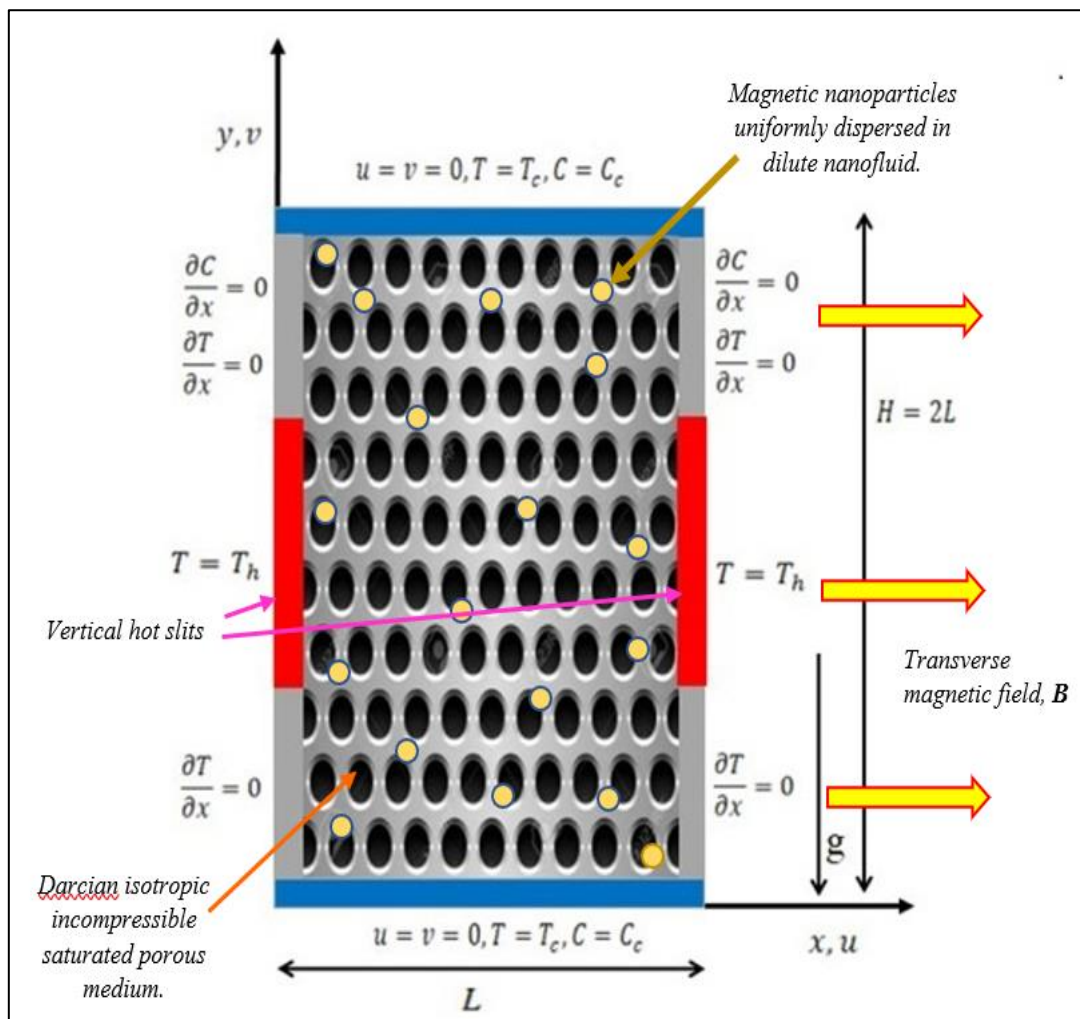


Fig. 1. 2-D model for electromagnetic nanofluid porous medium fuel cell

By incorporating the aforementioned assumptions, one can formulate the conservation (balance) equations for mass, momentum, energy and nanoparticle concentration. This involves combining and expanding upon earlier models in Sheremet *et al.* [9], Cimpean and Pop [11] and Venkatadri *et al.* [49] and Venkatadri [50]:

Mass conservation equation

$$\nabla \cdot \mathbf{V} = 0 \quad (1)$$

Momentum conservation equation

$$\begin{aligned} \rho_f \left[\frac{\partial \mathbf{V}}{\partial t} + (\mathbf{V} \cdot \nabla) \mathbf{V} \right] = & -\nabla p + \mu \nabla^2 \mathbf{V} - \frac{\mu}{\kappa} \mathbf{V} \\ & - \sigma (\mathbf{V} \times \mathbf{B}) \times \mathbf{B} + \beta \left[(C - C_c)(\rho_p - \rho_{f_0}) + (1 - C)\rho_{f_0}(T - T_c) \right] \mathbf{g} \end{aligned} \quad (2)$$

Energy conservation equation

$$\frac{\partial T}{\partial t} + (\mathbf{V} \cdot \nabla) T = \alpha \nabla^2 T + \delta \left[D_B \nabla C \cdot \nabla T + (D_T / T_c) \nabla T \cdot \nabla T \right] \quad (3)$$

Nanoparticles species conservation (mass diffusion) equation

$$\rho_p \left[\frac{\partial C}{\partial t} + (\mathbf{V} \cdot \nabla) C \right] = -\nabla \cdot \mathbf{j}_p \quad (4)$$

Here $\mathbf{j}_p = -\rho_p \left[D_B \nabla C + (D_T / T_c) \nabla T \right]$ is the nanoparticle mass flux, see Buongiorno [51] and Bég *et al.* [52]. The nomenclature at the beginning of the article specifies all remaining parameters. The specified initial and boundary conditions for dimensions are as follows:

$$\begin{array}{lll} \text{Top wall} & 0 \leq x \leq L, y = 2L & u = v = 0, T = T_c, C = C_c \end{array} \quad (5a)$$

$$\begin{array}{lll} \text{Bottom wall} & 0 \leq x \leq L, y = 0 & u = v = 0, T = T_c, C = C_c \end{array} \quad (5b)$$

$$\begin{array}{lll} \text{Left wall} & x = 0, 0 < y < \frac{2L}{3} & u = v = 0, \frac{\partial C}{\partial x} = 0, \frac{\partial T}{\partial x} = 0 \\ & x = 0, \frac{2L}{3} < y < \frac{4L}{3} & u = v = 0, T = T_h, C = C_h \\ & x = 0, \frac{4L}{3} < y < 2L & u = v = 0, \frac{\partial C}{\partial x} = 0, \frac{\partial T}{\partial x} = 0 \end{array} \quad (5c)$$

Right wall

$$\begin{aligned}
x=1, 0 < y < \frac{2L}{3} & \quad u = v = 0, \frac{\partial C}{\partial x} = 0, \frac{\partial T}{\partial x} = 0 \\
x=1, \frac{2L}{3} < y < \frac{4L}{3} & \quad u = v = 0, T = T_h, C = C_h \\
x=1, \frac{4L}{3} < y < 2L & \quad u = v = 0, \frac{\partial C}{\partial x} = 0, \frac{\partial T}{\partial x} = 0
\end{aligned}
\tag{5d}$$

In fluid dynamics, the vorticity-stream function formulation is an alternative way to describe the motion of an incompressible fluid, particularly for two-dimensional flow. This formulation is often used in the context of the Navier-Stokes equations. It is noteworthy that this formulation is specific to two-dimensional, incompressible flows and may not be as applicable in three-dimensional or compressible flow scenarios. To mitigate the contributions from pressure source terms, the vorticity–stream function formulation has been employed as per the following definitions:

$$\text{Stream function } u = \frac{\partial \bar{\psi}}{\partial y}, v = -\frac{\partial \bar{\psi}}{\partial x}, \quad \text{Vorticity } \bar{\omega} = \frac{\partial v}{\partial x} - \frac{\partial u}{\partial y}
\tag{6}$$

Next, the following dimensionless scaling variables are invoked [8]:

$$\tau = \frac{\alpha t}{L^2}, X = \frac{x}{L}, Y = \frac{y}{L}, \bar{\psi} = \frac{\psi}{\alpha}, \bar{\omega} = \frac{\omega L^2}{\alpha}, \theta = \frac{(T - T_c)}{(T_h - T_c)}, \phi = \frac{(C - C_c)}{(C_h - C_c)}
\tag{7}$$

Introducing eqn. (6) and (7) in Eqns. (1)-(4), the 2-D non-dimensional vorticity form of the transport equations emerge as follows:

$$\omega = -\frac{\partial^2 \psi}{\partial X^2} - \frac{\partial^2 \psi}{\partial Y^2}
\tag{8}$$

Momentum

$$\begin{aligned}
\frac{\partial \omega}{\partial \tau} + \frac{\partial \psi}{\partial Y} \frac{\partial \omega}{\partial X} - \frac{\partial \psi}{\partial X} \frac{\partial \omega}{\partial Y} = Pr \left[\frac{\partial^2 \omega}{\partial X^2} + \frac{\partial^2 \omega}{\partial Y^2} \right] - \frac{Pr}{Da} \omega + Ha^2 Pr \frac{\partial^2 \psi}{\partial X^2} \\
+ Ra.Pr \left(\frac{\partial \theta}{\partial X} - N \frac{\partial \phi}{\partial X} \right)
\end{aligned}
\tag{9}$$

Energy

$$\begin{aligned} \frac{\partial \theta}{\partial \tau} + \frac{\partial \psi}{\partial Y} \frac{\partial \theta}{\partial X} - \frac{\partial \psi}{\partial X} \frac{\partial \theta}{\partial Y} &= \frac{\partial^2 \theta}{\partial X^2} + \frac{\partial^2 \theta}{\partial Y^2} \\ &+ Nb \left(\frac{\partial \phi}{\partial X} \frac{\partial \theta}{\partial X} + \frac{\partial \phi}{\partial Y} \frac{\partial \theta}{\partial Y} \right) + Nt \left[\left(\frac{\partial \theta}{\partial X} \right)^2 + \left(\frac{\partial \theta}{\partial Y} \right)^2 \right] \end{aligned} \quad (10)$$

Nanoparticle concentration

$$\frac{\partial \phi}{\partial \tau} + \frac{\partial \psi}{\partial Y} \frac{\partial \phi}{\partial X} - \frac{\partial \psi}{\partial X} \frac{\partial \phi}{\partial Y} = \frac{1}{Le} \left(\frac{\partial^2 \phi}{\partial X^2} + \frac{\partial^2 \phi}{\partial Y^2} \right) + \frac{Nt}{Le Nb} \left(\frac{\partial^2 \theta}{\partial X^2} + \frac{\partial^2 \theta}{\partial Y^2} \right) \quad (11)$$

The significant non-dimensional parameters arising in Eqns. (7)-(10) are defined in **Table 1**:

The boundary conditions, which are dimensionless, are expressed in the following manner:

$$\begin{array}{lll} \text{Top wall} & 0 \leq X \leq 1, Y = 2 & \psi = 0, \omega = -\frac{\partial^2 \psi}{\partial Y^2}, \phi = 0, \theta = 0 \end{array} \quad (12a)$$

$$\begin{array}{lll} \text{Bottom wall} & 0 \leq X \leq 1, Y = 0 & \psi = 0, \omega = -\frac{\partial^2 \psi}{\partial Y^2}, \phi = 0, \theta = 0 \end{array} \quad (12b)$$

$$\begin{array}{lll} \text{Left wall} & X = 0, 0 < Y < \frac{2}{3} & \psi = 0, \omega = -\frac{\partial^2 \psi}{\partial X^2}, \frac{\partial \phi}{\partial X} = 0, \frac{\partial \theta}{\partial X} = 0 \\ & X = 0, \frac{2}{3} < Y < \frac{4}{3} & \psi = 0, \omega = -\frac{\partial^2 \psi}{\partial X^2}, \phi = 1, \theta = 1 \\ & X = 0, \frac{4}{3} < Y < 2 & \psi = 0, \omega = -\frac{\partial^2 \psi}{\partial X^2}, \frac{\partial \phi}{\partial X} = 0, \frac{\partial \theta}{\partial X} = 0 \end{array} \quad (12c)$$

$$\begin{array}{lll} \text{Right wall} & X = 1, 0 < Y < \frac{2}{3} & \psi = 0, \omega = -\frac{\partial^2 \psi}{\partial X^2}, \frac{\partial \phi}{\partial X} = 0, \frac{\partial \theta}{\partial X} = 0 \\ & X = 1, \frac{2}{3} < Y < \frac{4}{3} & \psi = 0, \omega = -\frac{\partial^2 \psi}{\partial X^2}, \phi = 1, \theta = 1 \\ & X = 1, \frac{4}{3} < Y < 2 & \psi = 0, \omega = -\frac{\partial^2 \psi}{\partial X^2}, \frac{\partial \phi}{\partial X} = 0, \frac{\partial \theta}{\partial X} = 0 \end{array} \quad (12d)$$

The local and average (mean) *Nusselt numbers and Sherwood number* are defined respectively as follows:

$$Nu = -\left(\frac{\partial \theta}{\partial Y} \right)_{Y=0,2} \quad \text{and} \quad Nu_{avg} = -\int_0^1 \left(\frac{\partial \theta}{\partial Y} \right) dX \quad (13)$$

$$Sh = -\left(\frac{\partial\phi}{\partial Y}\right)_{Y=0,2} \quad \text{and} \quad Sh_{avg} = -\int_0^1 \left(\frac{\partial\phi}{\partial Y}\right) dX \quad (14)$$

3. NUMERICAL SOLUTION AND VALIDATION

To accurately solve the vorticity-stream function equations (8)-(11), we employed a finite difference method under wall conditions (12). The numerical scheme adopted has been explained in detail by Venkatadri *et al.* [49]. Further examples of enclosure fluid dynamics simulations deploying this approach are given in [50, 52-54]. The stream function equation is solved with iterative method of Successive Overrelaxation (SOR). In the FDM computational code, we are used three-point central difference formulae and second order accuracy is achieved. The parabolic equations incorporate second-order accuracy through the discretization of diffusion terms using a central difference scheme. Simultaneously, convective terms are discretized using an alternative upwind difference scheme. The time derivative is handled with a first-order scheme. Finally, the vorticity at the boundaries is obtained by the help of Taylor series expansion.

Using the top wall as an example, from the equation (8), we know that

$$\omega_{i,N} = -\left.\frac{\partial^2\psi}{\partial Y^2}\right|_{i,N} \quad (15)$$

To obtain a finite difference approximation for the second-order derivative in the equation above, consider the Taylor series expansion:

$$\psi_{i,N-1} = \psi_{i,N} - \left(\frac{\partial\psi}{\partial Y}\right)_{i,N} dy + \left(\frac{\partial^2\psi}{\partial Y^2}\right)_{i,N} \frac{dy^2}{2} + \dots \quad (16a)$$

$$\text{For instance, } \left(\frac{\partial\psi}{\partial Y}\right)_{i,N} = U_{wall} \quad \text{and} \quad \left(\frac{\partial^2\psi}{\partial Y^2}\right)_{i,N} = \omega_{i,N}$$

By subbing these in and rearranging for vorticity we get:

$$\omega_{i,N} = 2\left(\frac{\psi_{i,N} - \psi_{i,N-1}}{dy}\right) - \frac{2U_{wall}}{dy} \quad (16b)$$

In similar manner, the other walls are addressed.

The present code has been benchmarked against several previous published investigations [21-23]. **Table 2** documents the comparison and evidently very close corroboration with previous studies is achieved, confirming the correctness of the present FDM code.

Table 1: Dimensionless control parameters for the model

Hartmann number	Ha	$B_0 H \sqrt{\frac{\sigma}{\mu}}$
Prandtl number	Pr	$\frac{\nu}{\alpha}$
Darcy number	Da	$\frac{K}{L^2}$
Rayleigh number	Ra	$\frac{(1 - C_c)\rho_{f0}g\beta(T_h - T_c)L^3}{(\mu\alpha)}$
Lewis number	Le	$\frac{\alpha}{D_B}$
Buoyancy ratio parameter	Nr	$\frac{(\rho_p - \rho_0)(C_h - C_c)}{(1 - C_c)\rho_{f0}\beta(T_h - T_c)L}$
Brownian motion parameter	Nb	$\frac{(\rho c_p)_p D_B (C_h - C_c)}{(\rho c_p)_f \alpha}$
Thermophoretic parameter	Nt	$\frac{(\rho c_p)_p D_T (T_h - T_c)}{(\rho c_p)_f \alpha T_c}$

Table. 2. The following results obtained from comparing the Average Nusselt number with other published works [55], [56], [57] for $Pr = 0.71$

Ra	Ref. [55]	Ref. [56]	Ref. [57] FEM	Present study
10^3	1.12	1.074	1.117	1.1185
10^4	2.243	2.084	2.254	2.2526
10^5	4.52	4.3	4.598	4.5907
10^6	8.8	8.743	8.976	8.9805

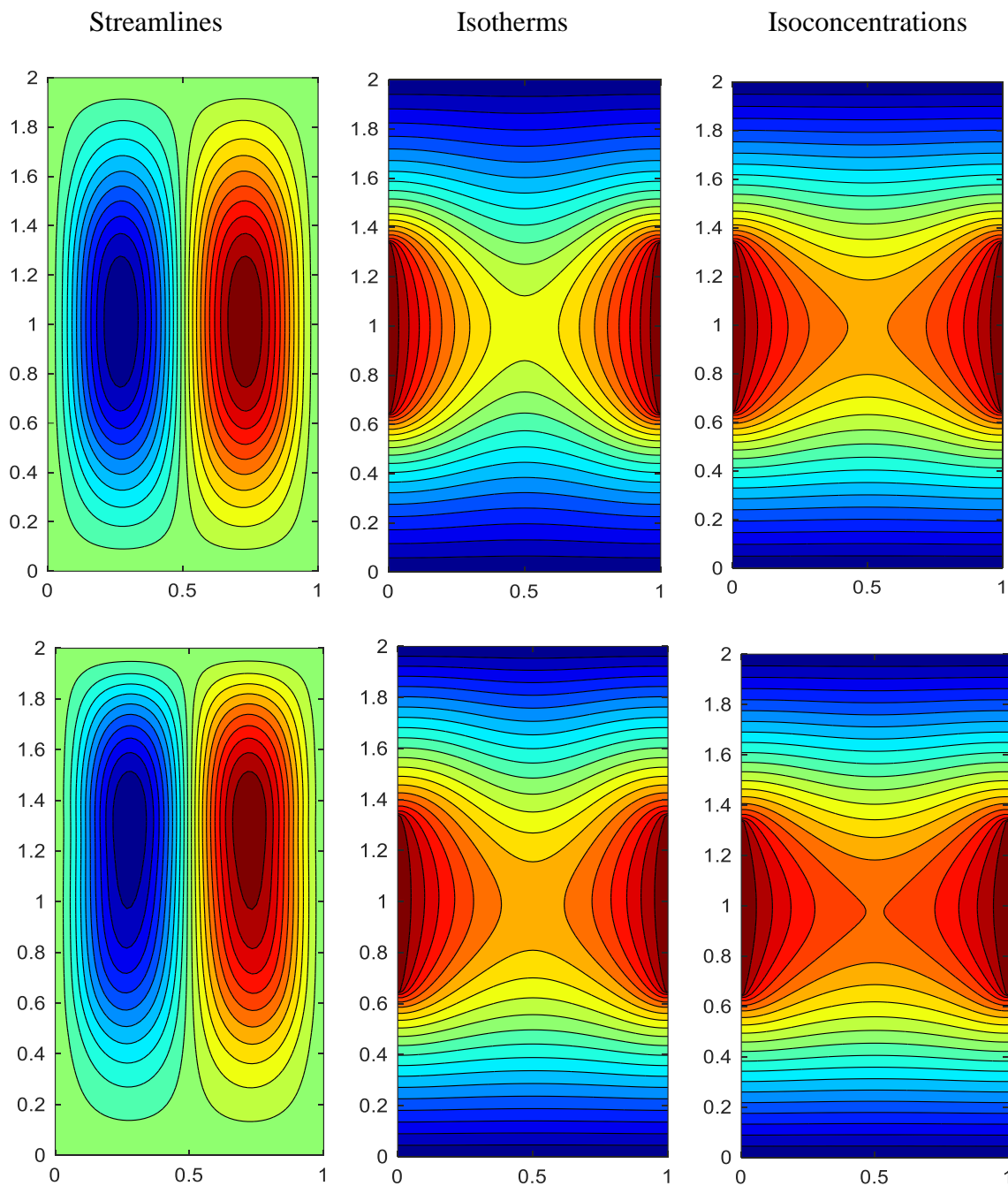


Fig. 2 Influence of Ra on streamline, isotherm and isoconcentration contours with $Pr = 6.2$, $Da = 0.01$, $Ha = 2$, $N = 1$, $Le = 1$, $Nt = 0.2$, $Nb = 0.3$ for $Ra = 10^3$ (top), and $Ra = 10^4$ (bottom).

4. NUMERICAL CONTOUR PLOTS, GRAPHS AND DISCUSSION

Figures 2- 9 Envision how various crucial factors, including the *buoyancy ratio parameter* (Nr), the *Lewis number* (Le), the *Darcy parameter* (Da), the *Schmidt number* (Sc), the *thermophoresis parameter* (Nt), the *Prandtl number* (Pr), the *Brownian motion parameter*

(Nb), and the Rayleigh number (Ra), on transport mechanism of conservation equations. The effects of these parameters were demonstrated through flow patterns, thermal distribution, and iso-concentrations. The following range of the three key parameters has been considered in the computations: Darcy number, $Da = 0.1, 0.01, 0.001, \text{ and } 0.0001$, Rayleigh number $Ra = 10^3, 10^4, 10^5 \text{ and } 5 \times 10^5$ and Hartmann number $Ha = 0, 2, 30 \text{ and } 50$. This data represents physically feasible fuel cell scenarios for actual porous media, thermal buoyancy effects and magnetic field intensities, and is extracted from Refs. [33]-[35], [42] and [45].

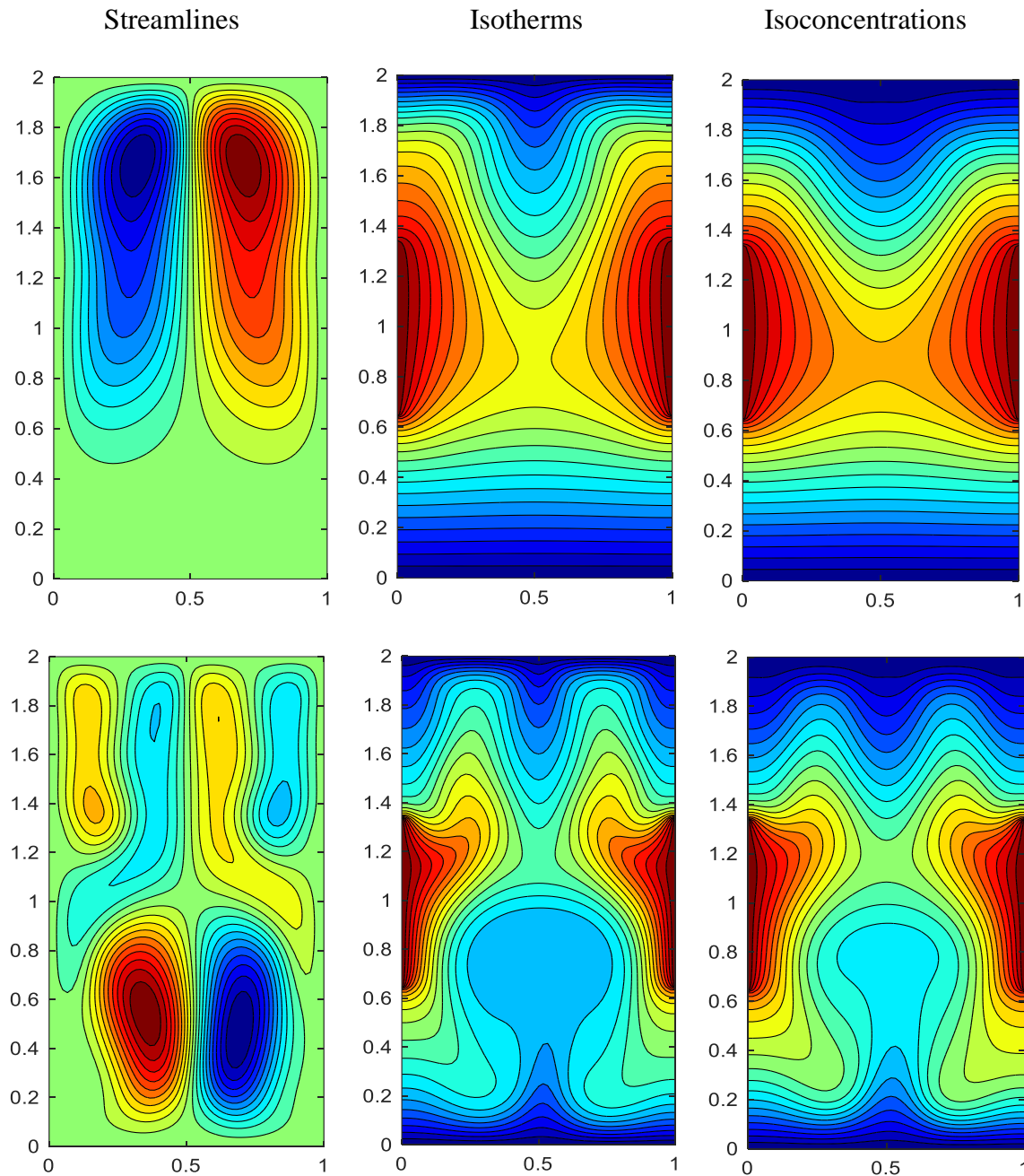


Fig. 3 Influence of Ra on streamline, isotherm and isoconcentration contours with, $Pr = 6.2$, $Da = 0.01$, $Ha = 2$, $N = 1$, $Le = 1$, $Nt = 0.2$, $Nb = 0.3$ for $Ra = 10^5$ (top), and $Ra = 5 \times 10^5$ (bottom).

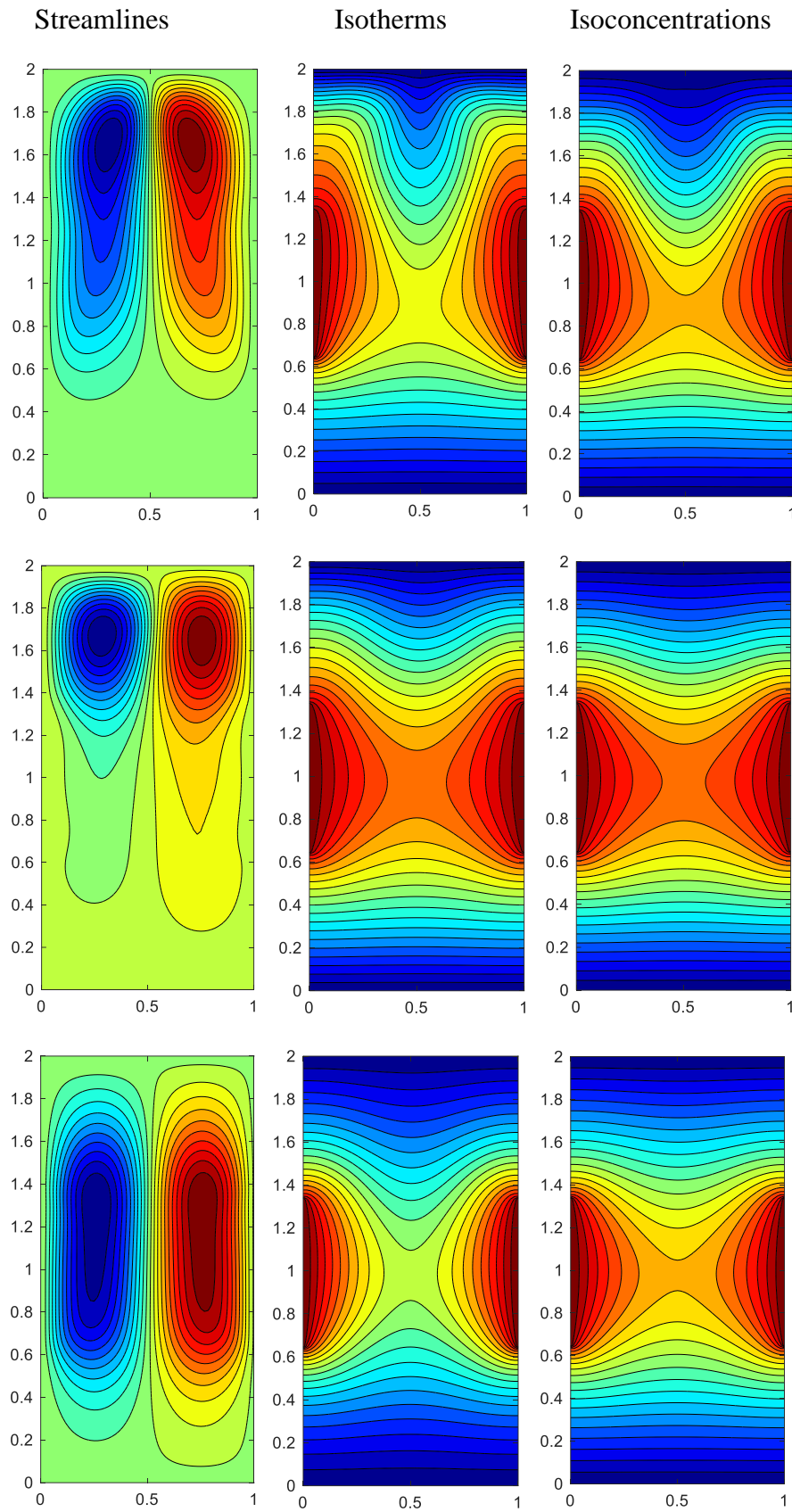


Fig. 4 Influence of Ha on streamline, isotherm and isoconcentration contours with $Pr = 6.2$, $Da = 0.01$, $N = 1$, $Le = 1$, $Nt = 0.2$, $Nb = 0.3$, $Ra = 10^5$ for $Ha = 0$ (top), $Ha = 30$ (middle), and $Ha = 50$ (bottom).

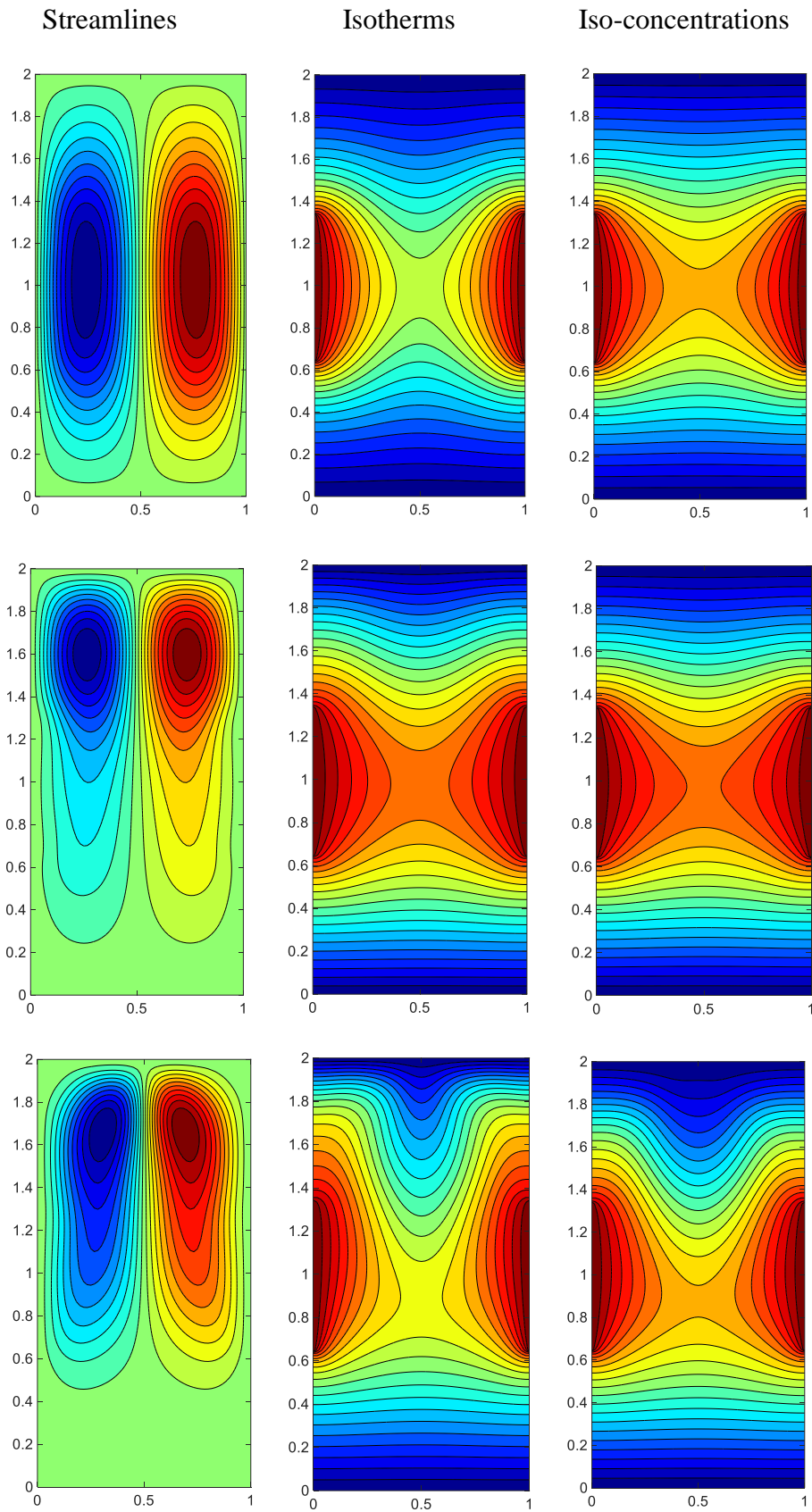


Fig. 5 Influence of Da on streamline, isotherm and isoconcentration contours with $Ra = 10^5$, $Pr = 6.2$, $Ha = 2$, $N = 1$, $Le = 1$, $Nt = 0.2$, $Nb = 0.3$. for $Da = 0.0001$ (top), $Da = 0.001$ (middle), and $Da = 0.01$ (bottom).

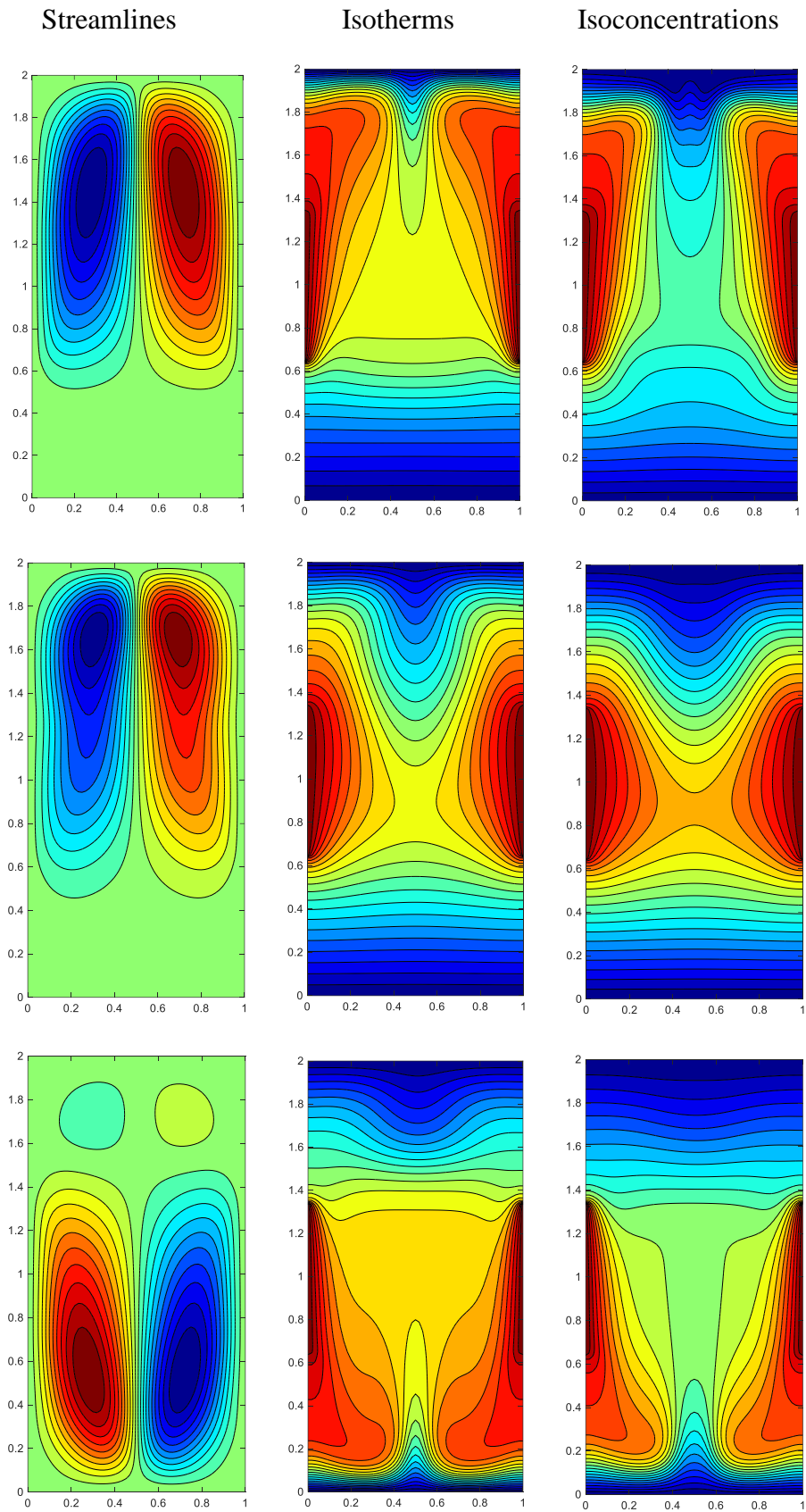


Fig. 6 Influence of N on streamline, isotherm and isoconcentration contours with $Ra = 10^5$, $Pr = 6.2$, $Ha = 2$, $N=1$, $Le = 1$, $Nt = 0.2$, $Nb = 0.3$, $Da = 0.01$ for $N=0$ (top), $N=1$ (middle), and $N=2$ (bottom).

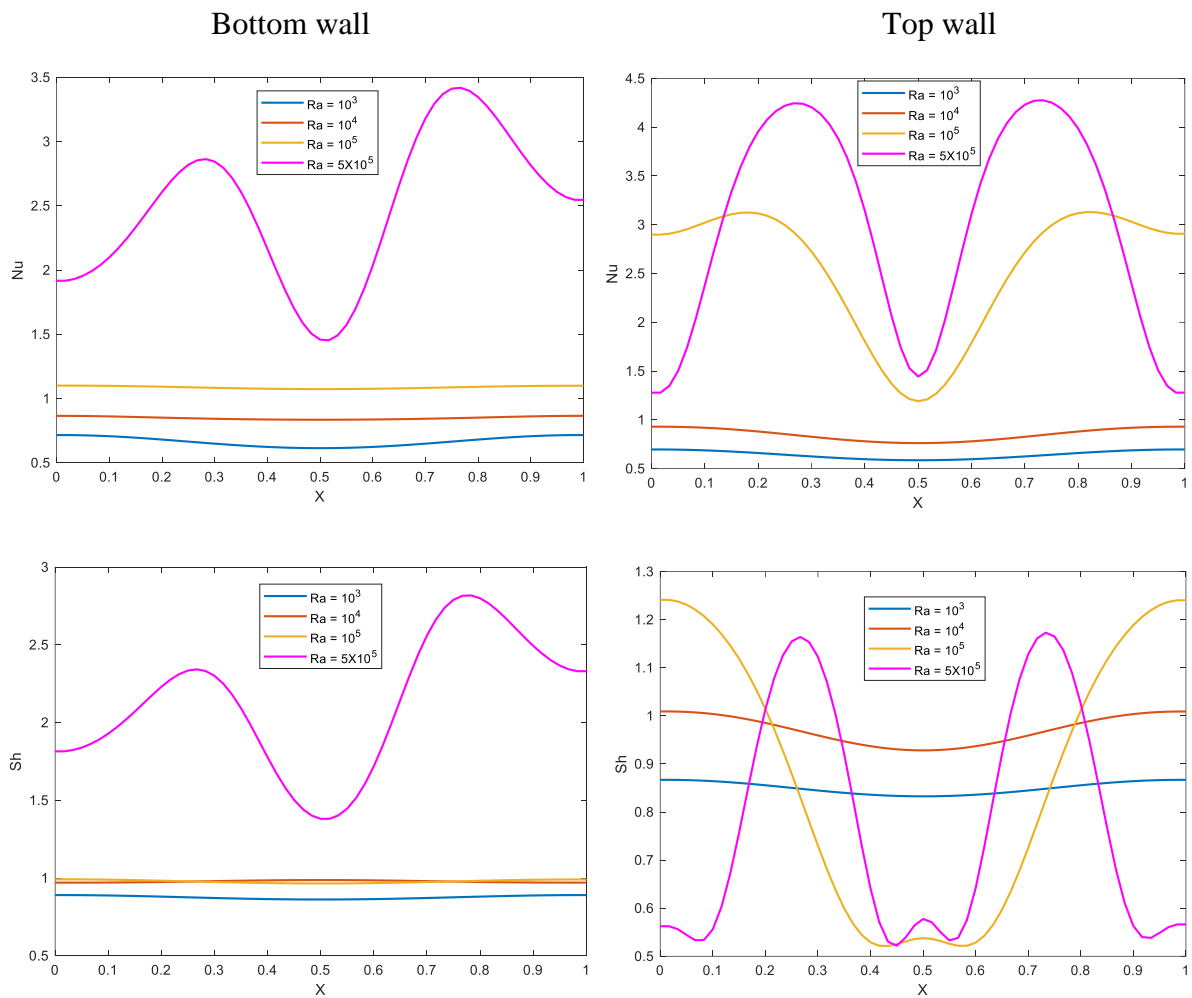
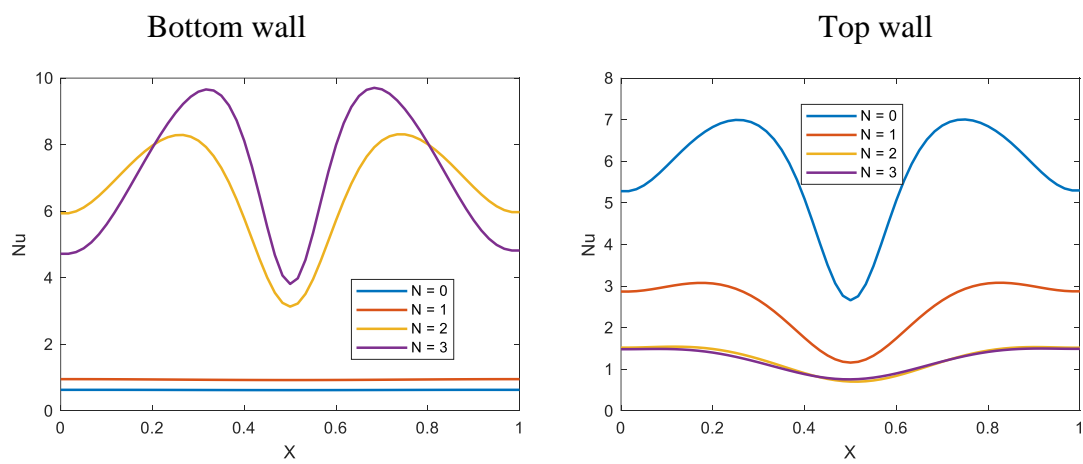


Fig. 7. Nusselt and Sherwood number along the bottom and top cold walls for *different Ra values* with $Pr = 6.2$, $Da = 0.01$, $Ha = 2$, $N = 1$, $Le = 1$, $Nt = 0.2$, $Nb = 0.3$.



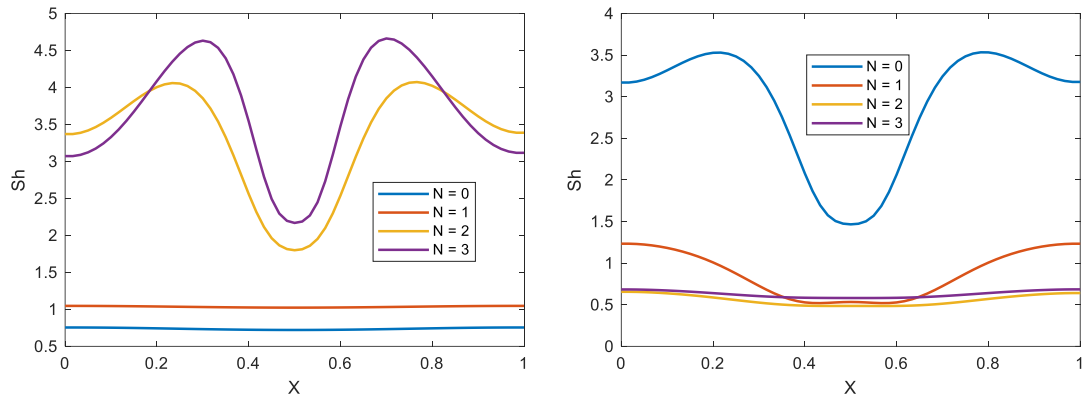


Fig. 8. Nusselt and Sherwood number along the bottom and top cold walls for different N values with $Pr = 6.2$, $Da = 0.01$, $Ha = 2$, $Le = 1$, $Nt = 0.2$, $Nb = 0.3$, $Ra = 10^5$.

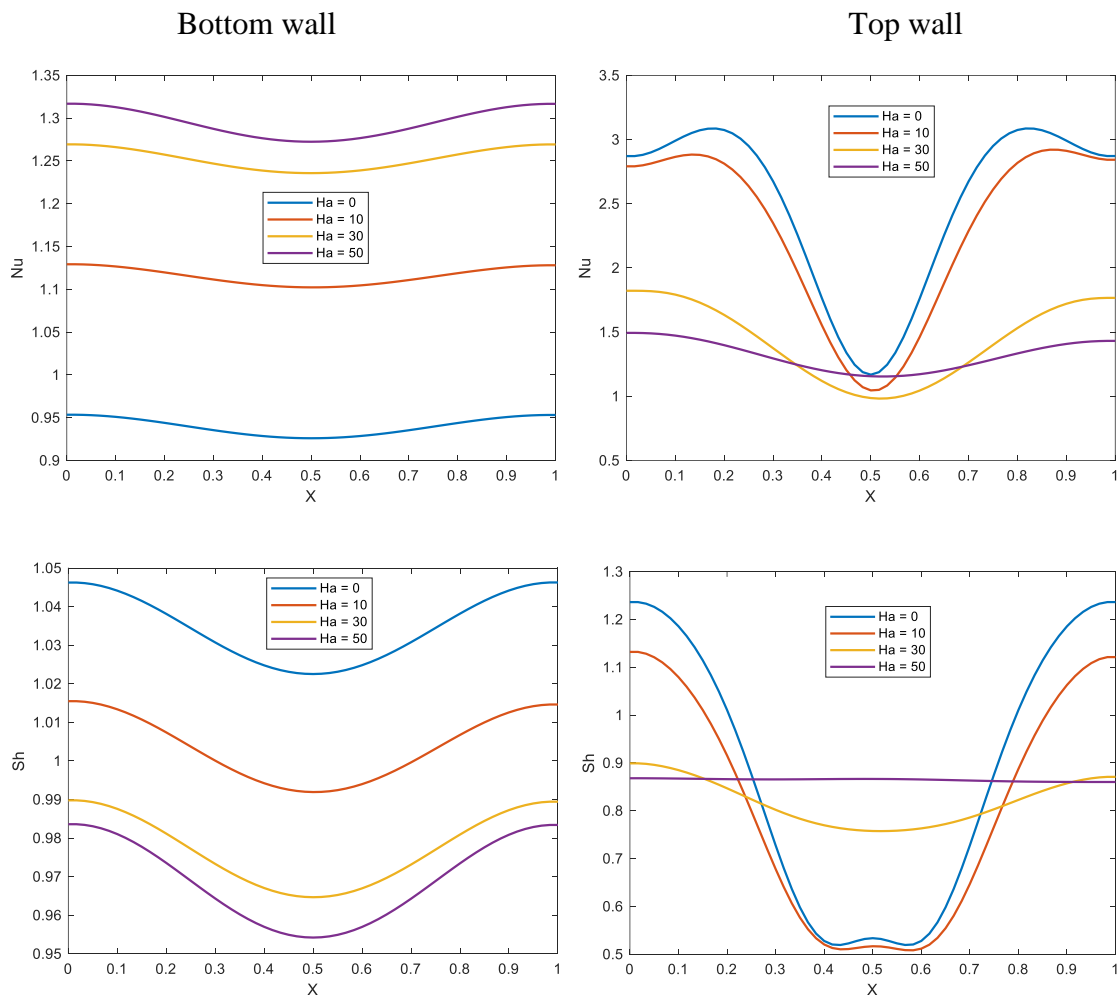


Fig. 9. Nusselt and Sherwood number along the bottom and top cold walls for different Ha values with $Pr = 6.2$, $Da = 0.01$, $N = 1$, $Le = 1$, $Nt = 0.2$, $Nb = 0.3$, $Ra = 10^5$.

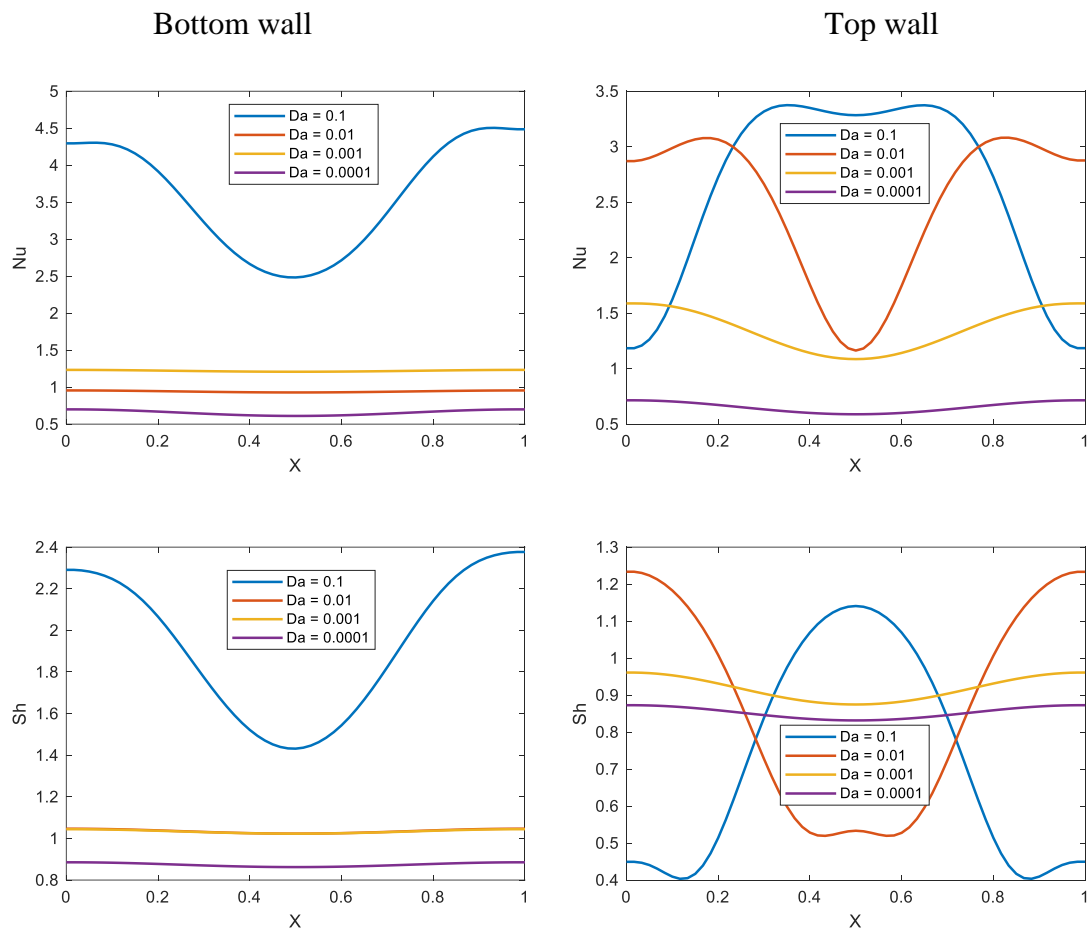
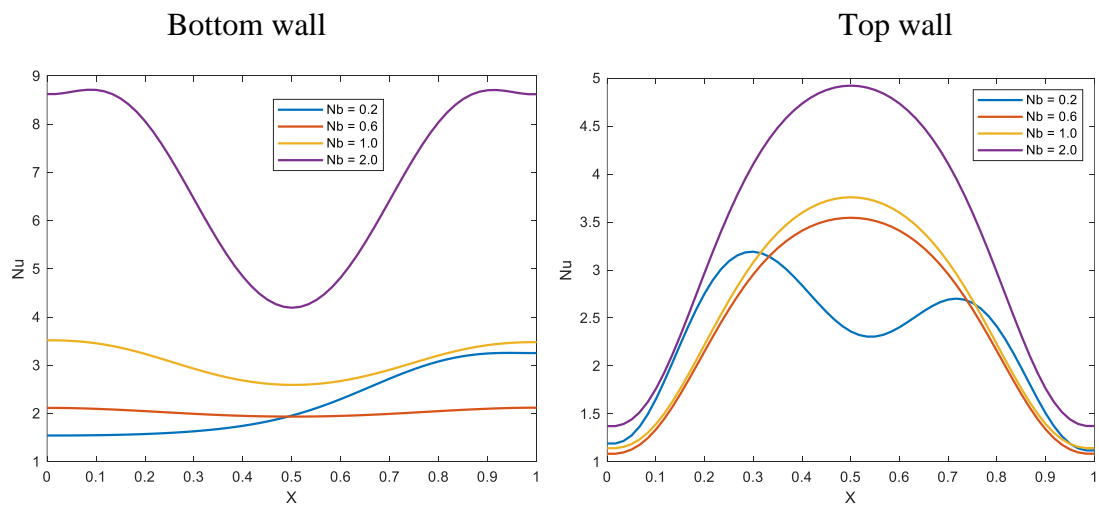


Fig. 10. Nusselt and Sherwood number along the bottom and top cold walls at different Da Values with $Pr = 6.2$, $Ha = 2$, $N = 1$, $Le = 1$, $Nt = 0.2$, $Nb = 0.3$, $Ra = 10^5$.



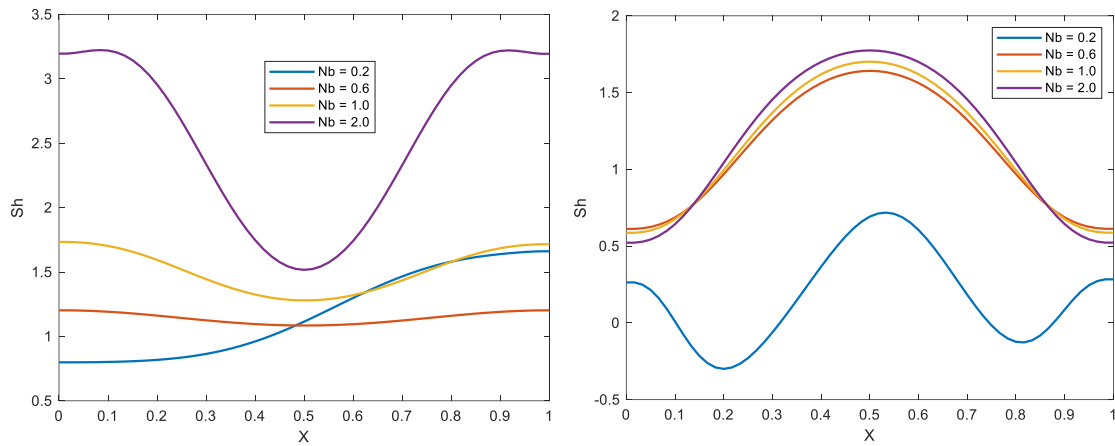


Fig. 11. Nusselt and Sherwood number along the bottom and top cold walls at different Nb values with $Ha = 2.0$, $Pr = 6.2$, $Da = 0.01$, $N = 1$, $Le = 1$, $Nt = 0.2$, $Ra = 10^5$.

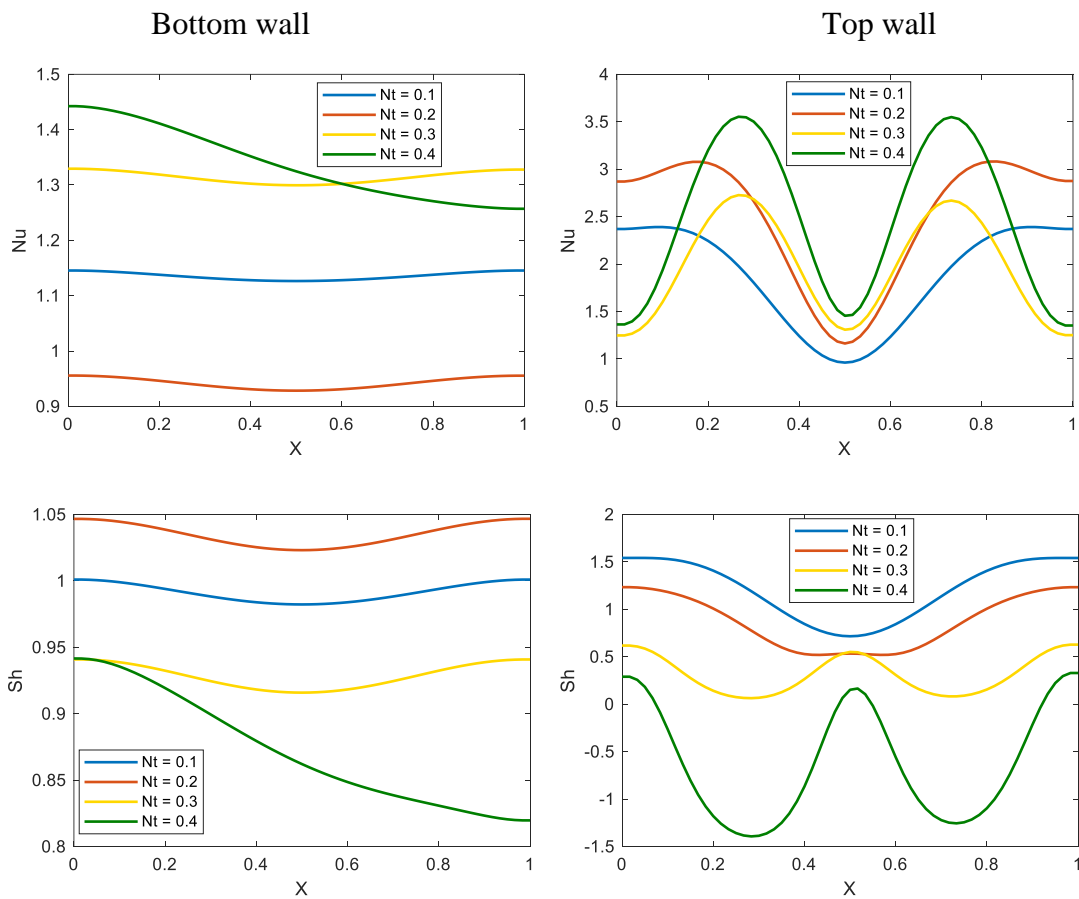


Fig. 12. Nusselt and Sherwood number along the bottom and top cold walls at different Nt values with $Ha = 2.0$, $Pr = 6.2$, $Da = 0.01$, $N = 1$, $Le = 1$, $Nb = 0.3$, $Ra = 10^5$.

Figure 2 demonstrates how the Rayleigh number influences flow patterns, temperature contours, and iso-concentration contours, with constant Hartmann number, Darcy parameter, Brownian motion, and thermophoresis ($Pr = 6.2$, $Da = 0.01$, $Ha = 2$, $N = 1$, $Le = 1$, $Nt = 0.2$, $Nb = 0.3$). Increasing the thermal Rayleigh number values indicates a buoyancy forces prevailing over viscous forces, leading to an improved thermal flow and the formation of more robust buoyancy flow currents within the enclosure regime. The fluid flow is weak in intensity with enlarged symmetrical circulations emerge close to the hot slits of the enclosure at low Rayleigh numbers ($Ra = 10^3$) with their respective thermal contours and iso-concentrations running parallel to the cold walls. The presence of opposing temperature and concentration gradients results in the formation of symmetric convective cells confined within the enclosure. Furthermore, as the thermal buoyancy force is augmented, transitioning from $Ra = 10^3$ to $Ra = 10^4$, the fluid flow patterns undergo a notable morphing, and becoming increasingly orientated upward towards the upper cold wall. Simultaneously, both the isotherms and iso-concentrations transition from a parallel configuration to a slightly distorted nature. This nuanced evolution in flow dynamics and concentration patterns underscores the intricate interplay between temperature gradients and transport characteristics within the given enclosure. The strength of the symmetric circulation intensifies as the Ra increases. Furthermore, the observed isotherms and iso-concentrations provide evidence that the average fluid temperature and concentration within the enclosure are elevated in magnitude proportionally with greater buoyancy force present.

Figure 3 shows that significant changes in fluid flow circulations, isotherm contours and iso-concentrations are observed at $Ra = 10^5$ and $Ra = 10^5$, with constant Hartmann number, Darcy parameter, Brownian motion, and thermophoresis ($Pr = 6.2$, $Da = 0.01$, $Ha = 2$, $N = 1$, $Le = 1$, $Nt = 0.2$, $Nb = 0.3$). Rayleigh number features in the composite thermal/species buoyancy force term, $+Ra.Pr \left(\frac{\partial \theta}{\partial x} - N \frac{\partial \phi}{\partial x} \right)$ in eqn. (9). Marked alterations in the circulation patterns of fluid flow, temperature distribution, and iso-concentration levels become evident when the Rayleigh number attains a value of 10^5 . At this Rayleigh number, the fluid flow circulation experiences an elevation attributed to the intensified buoyancy forces which encourage momentum development. This results in the formation of two symmetric circulations near the upper cold wall. Concurrently, the isotherms and iso-concentrations exhibit fluctuations in proximity to the upper cold wall, whereas they maintain a parallel configuration near the lower cold wall. Significant changes in the way magnetic nanofluid circulates within the enclosure, the distribution of temperature and the distribution of

nanoparticles (concentrations) become apparent when the Ra is further increased to the maximum value of 5×10^5 . At this specific Rayleigh number, the amplification in thermal buoyancy forces lead to the creation of multiple fluid flow structures within the enclosure, and strongly intensifies circulation. This, in turn, gives rise to two prominent symmetric flow circulations (vortex cells) near the lower cold wall. Simultaneously, the temperature and concentration levels curves demonstrate oscillating behaviour along the cold walls, reflecting dynamic variations in temperature and concentration in these locations.

Fig. 4 visualizes the distributions of streamlines (constant velocity contours), isotherms, iso-concentrations with an increment in Hartmann number, Ha , for $Pr = 6.2$, $Da = 0.01$, $N = 1$, $Le = 1$, $Nt = 0.2$, $Nb = 0.3$, $Ra = 10^5$. Hartmann number features inly in the Lorentzian force term, $+Ha^2 Pr \frac{\partial^2 \psi}{\partial x^2}$ in the momentum eqn. (9). As Ha is enhanced, the impact of magnetic forces becomes more pronounced compared to the prevailing viscous force. The intensification in Lorentzian magnetohydrodynamic drag force associated with the larger Hartmann number results in a significant boost in heat and solute (nanoparticle) diffusion through the damping (deceleration) in the velocity field. Therefore, while momentum is inhibited the heat and nanoparticle diffusion are amplified. At a Hartmann number (Ha) of 50, the isotherms align parallel to the enclosure's horizontal walls, signifying the prevalence of conduction over convection. As the Hartmann number decreases, Lorentzian magnetic drag is depleted, and the symmetric circulation intensifies. Additionally, the average fluid and solutal temperature within the circulating magnetic nanofluid in the cavity exhibit elevating magnitudes. This increase is accompanied by reduced flow obstruction due to the Lorentz force acts perpendicular to the direction of the magnetic field, and the fluctuation in the isotherms becomes more pronounced at lower Hartmann numbers (Ha). In the absence of magnetic field ($Ha = 0$), the damping effect of the Lorentzian magnetic body force vanishes and more intensive circulation in the magnetic nanofluid is observed with in the enclosure. For this electrically non-conducting case, the convection effect intensifies even more, primarily attributed to the heightened momentum diffusion. The isotherms and iso-concentrations are significantly compressed near the upper region of the rectangular enclosure due to intensified convection from both the hot slits and the upper cold wall.

In **Figure 5**, the impact of Da on the streamline pattern, temperature and iso-concentrations contours within the rectangular enclosure is visualized. An upsurge in nanoparticle concentration may alter the effective internal resistance of a fluid to flow and

thermal conductivity of the nanofluid, impacting its flow through the porous medium. Darcy number arises in the term, $-\frac{Pr}{Da}\omega$, in the vorticity momentum eqn. (9). In convective nanofluid flow, the variation in temperature across different areas is significant. As the porosity escalates to $Da = 0.0001$, the permeability of the porous medium undergoes a remarkable tenfold increase. This substantial augmentation results in a significantly expanded void space, facilitating enhanced percolation of the magnetic nanofluid. Concurrently, there is a corresponding reduction in resistance posed by the solid matrix fibers to internal circulation. Streamlines ease at the upper cold wall, while the hot zone is restricted in the proximity of the left and right walls (hot slits). Robust symmetry is discernible in the topologies for isotherms and iso-concentrations. Elevated Darcy numbers lead to the repression of thermal conduction at the enclosure's periphery, thermal and solutal diffusion intensify, prompting the hot zone to expand progressively in the central region of domain. This culminates in a substantial alteration in temperature and iso-concentration distribution within the enclosure, presenting noteworthy advantages for fuel cell designs. In general, at low Darcy numbers ($Da = 0.0001$), the streamlines exhibit a predominantly vertical orientation. Due to the low permeability, there is a deceleration within the primary flow. As permeability increases ($Da = 0.001$), the streamlines undergo distortion and become constrained towards both the upper and lower cold walls, leading to asymmetrical patterns. The streamlines then relax near the upper cold wall. Initially confined to the vicinity of the left and right walls (hot slits), the hot zone exhibits strong symmetry in both isotherms and iso-concentration. As the Darcy number rises, a distinct reduction in thermal conduction becomes evident around the periphery of the enclosure. This reduction is due to the gradual decrease in the number of solid fibres in the porous material. Conversely, in the middle zone, both thermal and nanoparticle species diffusion become more pronounced, leading to the extension of the hot core towards the middle region of the domain. An increased permeability of the porous medium, therefore, brings about significant alterations in temperature and iso-concentration distribution within the enclosure.

Figure 6 demonstrates how the buoyancy ratio parameter (N) affects the flow pattern, temperature distribution and nanoparticle species concentration within the rectangular enclosure. This is shown for a particular set of conditions where $Ra = 10^5$, $Pr = 6.2$, $Ha = 2$, $N = 1$, $Le = 1$, $Nt = 0.2$, $Nb = 0.3$, $Da = 0.01$. Within these computations, the Hartmann magnetic drag force exerts a magnitude that is twice that of the viscous hydrodynamic force. The buoyancy ratio parameter N plays a crucial role in regulating the heat transfer, fluid flow behaviour and nanoparticle concentration profiles. The coupling buoyancy term is responsible

for causing the mentioned effect, $-Ra \cdot Pr \left(N \frac{\partial \phi}{\partial x} \right)$ in the momentum eqn. (9). The contour plots reveal a red-hot zone and a blue cold area, indicating the temperature distribution within the enclosure. Interestingly, at $N = 1$ and $N=2$, opposite fluid flow patterns and thermal and solutal distributions are observed. As the buoyancy ratio parameter increases, the thermal and solutal plumes along the top cold wall gradually diminish, and the symmetrical fluid flow circulation near the middle of the boundary is displaced towards the bottom wall due to the opposing buoyancy ratio parameter. This shift has a considerable effect on the transfer of momentum within the cavity and significantly modifies vortex structures.

Figures 7-12 provide a depiction of the local heat and mass transport rate along both cold walls as a function of several key control parameters. In Figure 7, it can be observed that an increase in thermal Rayleigh number (Ra) results in a notable enhancement of heat transfer and nanoparticle solutal transport. This is due to the dominance of thermal buoyancy over viscous resistive force, which intensifies the convection currents in the regime and encourages both mass and species diffusion out of the enclosure bulk fluid to the external walls. The stronger buoyancy forces stimulate significant acceleration in the percolating magnetic nanofluid flow and via coupling of the energy (8) and nanoparticle concentration fields (9) to the momentum eqn. (7), thermal and solutal diffusion to the boundaries is also accentuated in the porous medium. Therefore, both Nusselt's and Sherwood's numbers are boosted. Nusselt and Sherwood numbers along the top cold wall are observed to have an inverse Gaussian curve nature. In contrast, a greater value of Rayleigh number modifies the topologies to a hybrid inverse Gaussian curve nature. **Figure 8** presents insights into the impact of the buoyancy ratio parameter N on Nusselt and Sherwood numbers at the cold walls. Evidently an increase in N results in a significant rise in both numbers indicating that greater heat flux and nanoparticle species transport to the boundaries is produced. Specifically, for $N=0$, the movement is entirely propelled by the force of thermal buoyancy, and the species-induced buoyancy force vanishes for this scenario. However, as N grows larger, the buoyancy forces caused by thermal and species opposition also increase, particularly with regards to nanoparticle concentration leads to complex and intricate flow patterns. The oscillatory nature of the profiles is also suppressed with increasing buoyancy ratio parameter. Furthermore, an intriguing reversing transport mechanism is observed as the buoyancy ratio parameter N increases. The impact of the Hartmann magnetic parameter (Ha) on the local Nusselt and Sherwood numbers along the cold walls is illustrated in **Figure 9**. There is a notable impact caused by the magnetic field on the rates of thermal and solutal transport to the cold walls. A stronger magnetic field produces a

decrease in both heat and nanoparticle mass transfer rates, with distance x along the walls. At higher Ha values, the Lorentz magnetic drag is more dominant than the viscous force in the regime. Both body forces exert an equivalent influence for the case when $Ha = 1$. The maximum Nusselt and Sherwood numbers are achieved without a transverse magnetic field ($M = 0$) i. e. for electrically non-conducting nanofluid. This is consistent with the higher isotherm and isoconcentration magnitudes computed in earlier figures, within the enclosure, which are minimal with vanishing magnetic field but maximum with weak magnetic field. External magnetic field therefore has the opposite impact on momentum transfer compared with heat and nanoparticle mass transfer. The insights from **Figure 10** are quite valuable as they reveal how the increase in Darcy number (Da) can considerably influence the local Nusselt and Sherwood numbers along the lower cold boundary of the enclosure. It is observed that both are highest at the left vertical wall ($X = 0$) or right vertical wall ($X = 1$) for maximum Darcy number i. e. $Da = 0.1$ However the Nusselt number magnitudes are significantly greater than Sherwood numbers. The presence of the Darcy number in the Darcian drag force e.g. $-\frac{Pr}{Da}\omega$ in the momentum transport equation (7) leads is clearly as a denominator. This influences strongly the momentum diffusion and circulation in the enclosure and via coupling an indirect effect is experienced by the temperature and nano-particle concentration. However, the effect at the top wall is different – here the maximum Darcy number produces maximum Nusselt number at the mid-point location along the wall, not at the peripheries (vertical boundaries). The profiles are significantly more oscillatory in nature than for the bottom wall. Similarly, the Sherwood number is influenced differently at the bottom wall compared with top wall with a change in Darcy number. As with Nusselt number, the Sherwood number peaks for maximum Darcy number at the peripheries ($X=0, 1$) at the bottom wall but attains a maximum only at the central location of the top wall. At the bottom wall with lower Darcy number the Nusselt number and Sherwood number are both suppressed and profiles are essentially linear. However, at the top wall the response in Nusselt and Sherwood numbers is more erratic at lower Darcy numbers and exhibits a periodic nature (undulations) along the length of the wall. Clearly the nature of the thermal and nanoparticle diffusive flux to the two horizontal walls of the enclosure undergoes a complex modification due to the permeability of the porous medium. **Figs. 11 and 12** depict the effects of the Buongiorno nanoscale parameters i. e. *Brownian motion* (Nb) and *thermophoresis* (Nt) parameters, respectively on Nusselt and Sherwood number distributions along the base and upper boundaries. When the value of the Brownian motion parameter (Nb)

increases, there is generally a consistent enhancement in thermal and solutal transport rates to both walls. However, the nature of the profiles is very different. At the bottom wall for maximum $Nb = 2.0$, the profile is parabolic whereas at the upper wall it exhibits an inverted parabolic topology. As Nb is reduced, the bottom wall Nusselt number profiles are essentially damped out, become linear at $Nb = 0.6$ and then resume a sigmoidal pattern at $Nb = 0.2$. In this last case the peak Nusselt number arises at the right vertical wall, $X = 1.0$ whereas for $Nb = 1.0$ and 0.6 , peaks are computed at both the vertical walls. For $Nb = 2.0$, the peaks are slightly displaced from the vertical walls, and a minimum is computed at the centre of the wall ($X = 0.5$); these minimums echo the behaviour at $Nb = 1.0$ and 0.6 . At the top wall however, generally for $Nb = 2.0, 1.0$ and 0.6 , a classical parabolic distribution is computed along the wall with peak Nusselt number always arising at the centre ($X = 0.5$); only for the minimal Nb case (0.2) is an oscillatory pattern computed with the higher peak at $X \sim 0.3$ and the lower peak at $X \sim 0.7$. In all cases, the minimum Nusselt number is observed at the left and right vertical walls. The Sherwood number plots at the bottom and top walls resemble the Nusselt number plots, although magnitudes are significantly smaller. Also, the Sherwood number distributions are much more constricted at the upper wall for $Nb = 2.0, 1.0, 0.6$ and for $Nb = 0.2$, again a strongly oscillatory nature is observed, and three peaks are computed – *two lower peaks at the left and right walls and the maximum peak at the central zone*. The Brownian motion parameter features in the augmented diffusion term, $+Nb \left(\frac{\partial \phi}{\partial X} \frac{\partial \theta}{\partial X} + \frac{\partial \phi}{\partial Y} \frac{\partial \theta}{\partial Y} \right)$ in the energy conservation eqn. (10) and also in the coupling term, $+\frac{Nt}{LeNb} \left(\frac{\partial^2 \theta}{\partial X^2} + \frac{\partial^2 \theta}{\partial Y^2} \right)$ in the nanoparticle concentration eqn. (11). In the former term there is a direct proportionality with Brownian motion parameter whereas in the latter there is an inverse relationship. Brownian motion relates to the haphazard motion of nanoparticles in the magnetic nanofluid. It is associated with micro-convection effects and also influences thermal conduction. In the Buongiorno model [1], larger values of Nb correspond to smaller sized nanoparticles and vice versa for smaller values of Nb . As Nb is increased, the smaller nanoparticles produce less ballistic collisions which act to de-energize the nanofluid. This reduces temperatures within the enclosure but enhances the net heat transferred to the boundaries. Nusselt number is therefore elevated as observed in **Fig. 10** with an increment in Brownian motion parameter. Similar remarks have been noticed by Azizul *et al.* [46] and Sumithra *et al.* [47], among others, for electromagnetic nanofluid flows in cavity systems. **Figures 11 and 12** exhibit the response in Nusselt number and Sherwood number profiles with thermophoresis parameter, Nt . This is also a key nanoscale parameter in the Buongiorno model pertains to the movement of nanoparticles in the presence of a powerful

thermal gradient. This model is characterized by the augmented diffusion term, $+Nt \left[\left(\frac{\partial \theta}{\partial X} \right)^2 + \left(\frac{\partial \theta}{\partial Y} \right)^2 \right]$ in the energy conservation eqn. (10) and as with the Brownian motion parameter, Nb , also in the coupling term, $+\frac{Nt}{LeNb} \left(\frac{\partial^2 \theta}{\partial X^2} + \frac{\partial^2 \theta}{\partial Y^2} \right)$ in the nanoparticle concentration eqn. (11). With increment in Nt values, (**Figure 11**) generally the Nusselt numbers at both bottom and top walls are strongly enhanced. The thermophoretic body force drives the heat towards the cooler boundaries. This elevates the Nusselt number and peaks are observed at the left wall (for $Nt = 0.4$, the maximum value), whereas peaks are present at both the left and right walls for $Nt = 0.3, 0.2, 0.1$. These three cases all demonstrate steady response across the wall, whereas the $Nt = 0.4$ case shows a monotonic decay with the minimal Nusselt number at the right wall. The case of the top wall shows very different Nusselt Number topologies. While Nusselt number does invariably increase with greater Nt values, the profiles are oscillatory and double peaks are computed around the wall central zone ($X = 0.5$). The relationship between thermophoresis and the nanoparticle behaviour is clearly intricate and complex. At different locations along the upper wall, different behaviours are computed. **Figure 12** reveals that Sherwood numbers along the bottom wall are conversely suppressed strongly with an increase in thermophoresis parameter. The stronger temperature gradient induced by thermophoretic body force amplification (increasing Nt values), encourages heat flux to the colder wall but inhibits the diffusion of the nanoparticles. This reduces the Sherwood number at the wall since nanoparticle concentrations within the magnetic nanofluid circulating the enclosure are elevated whereas the net transport of nanoparticles towards the boundary (bottom wall) is curbed. Inevitably this will also influence the boundary layer thickness at the boundary, although more detailed numerical simulations will be needed to reveal the complex structures there. At the upper wall, as with Nusselt number, undulating topologies are computed for Sherwood number. However there is a much more consistent response to decrement in Nt values- nanoparticle mass transfer flux to the upper wall is depleted. Dual peaks are computed again around the mid-point of the upper wall for lower values of $Nt = 0.1, 0.2$, whereas for higher values i. e. $Nt = 0.3, 0.4$, the topologies morph. In these latter two cases, the peak Sherwood number migrate to the centre point ($X = 0.5$) of the upper wall and also arise at both the left and right vertical walls. The sensitivity of the thermal and mass diffusion phenomena to both nanoscale parameters is clearly captured in **Figs. 11 and 12**.

5. CONCLUSIONS

A laminar magneto-hydrodynamics (MHD) mathematical model has been developed to analyze natural convection in a rectangular enclosure. The enclosure contains a permeable medium filled with incompressible electro-conductive Buongiorno nanofluid. The model incorporates the effects of thermophoresis and Brownian motion and uses a Darcian drag force model for the isotropic porous medium. The solutions have been validated for average Nusselt number at the top wall, and the influence of critical parameters on streamline flow patterns, temperature, iso-concentration, and local Nusselt and Sherwood numbers (at the base and upper walls) have been computed and illustrated graphically. The simulation has shown that:

- (i) The Nusselt numbers have significantly increased on both the top and bottom walls with an increment in Buongiorno nanoscale thermophoresis parameter.
- (ii) Sherwood numbers along the bottom wall are depleted strongly with an increase in Buongiorno nanoscale thermophoresis parameter.
- (iii) Increasing the Buongiorno nanoscale Brownian motion parameter generally enhances local Nusselt and Sherwood numbers at both cold walls of the enclosure. However, the topologies of the profiles are very different. The Sherwood number plots at the bottom and top walls resemble the Nusselt number plots, although magnitudes are substantially lower.
- (iv) Elevation in buoyancy ratio parameter (N) enhances both Nusselt and Sherwood numbers at the upper and lower cold walls, implying that greater heat flux and nanoparticle species transport to the boundaries is produced. For $N=0$, thermal buoyancy force solely drives the flow, and species-induced buoyancy force vanishes. However, as the value of N increases, opposing thermal and species (nanoparticle concentration) buoyancy forces lead to complex and intricate flow patterns. The oscillatory nature of the profiles is also damped with increasing buoyancy ratio parameter.
- (v) Higher Hartmann (magnetic field) number values, on the other hand, lead to a reduction in local Nusselt number profiles but have a weaker influence on local Sherwood number.
- (vi) The permeability of the porous medium, as simulated via the Darcy number, has a strong impact on streamlines, isotherms, and iso-concentrations. With greater permeability i. e. When the Darcy number is increased, the flow lines become highly distorted and more tightly arranged towards the upper and lower cold walls,

leading to uneven distributions. The flow lines tend to ease off near the upper cold wall.

- (vii) A reduction in Darcy number suppresses local Nusselt and Sherwood numbers, whereas an elevation in Rayleigh number enhances them.

The present finite difference computational fluid dynamics simulations have furnished some interesting observations on the circulation and thermal/solutal behaviour of magnetized nanofluids in two-dimensional enclosures, smart nanomaterial processing systems and hybrid electromagnetic nano-liquid fuel cells serve as models for advanced technological solutions. However, attention has been confined to purely Lorentzian magnetohydrodynamics and has ignored the effects of *electromagnetic induction and also magnetic dipole phenomena* [58], both of which are of relevance to optimizing hybrid electromagnetic nanofluid fuel cell performance. Additionally, only *Newtonian* magnetic nanofluids have been considered, and specific nanoparticle types ignored. Future pathways include exploring non-Newtonian (e.g., micropolar [59]) magnetized nanofluids and utilizing the Tiwari-Das or Maxwell-Garnetts volume fraction nanoscale models to consider specific metallic/carbon nanoparticles e. g. gold, silver, zinc, graphene, graphite, diamond, cobalt oxide etc [60] and also different geometries e. g. hexagonal and octagonal and furthermore, *geometrical aspect ratio* effects [61]. These aspects are under consideration, and the finite difference scheme appears to be versatile enough to accommodate these complexities. Plans regarding these initiatives will be communicated in the near future.

CONFLICT OF INTEREST

The author does not have any financial or personal conflicts of interest that could potentially influence the content or findings presented in their work.

NOMENCLATURE:

Roman

B_0 Magnetic field strength $[kg\ s^{-2}\ A^{-1}]$

C Dimensional concentration of the fluid $[kg\ m^{-3}]$

C_c Low concentration $[kg\ m^{-3}]$

C_h	High concentration [$kg\ m^{-3}$]
D_T	Thermophoresis diffusion coefficient [m^2s^{-1}]
Da	Darcy number [-]
g	Acceleration due to gravity [ms^{-2}]
Gr	Grashof number [-]
H	Height of the enclosure [m]
Ha	Hartmann number [-]
K	Permeability of the porous medium [m^2]
L	Length of the cavity [m]
N_T	Thermophoresis parameter [-]
N_B	Brownian motion parameter [-]
Nu	Local Nusselt number [-]
N	Buoyancy ratio parameter [-]
p	Dimensional pressure [Pa]
P	Dimensionless pressure [-]
Pr	Prandtl number [-]
Ra	Rayleigh number [-]
Sc	Schmidt number [-]
t	Dimensional time [s]
T	Dimensional temperature of the fluid [K]
T_h	Temperature of the hot wall [K]
T_c	Temperature of the cold wall [K]
U, V	Dimensionless velocities along X and Y directions [-]
u, v	Dimensional velocity components in x and y directions [ms^{-1}]
U_0	Constant reference velocity [ms^{-1}]
X, Y	Dimensionless Cartesian coordinates [-]
x, y	Dimensional Cartesian coordinates [m]

Greek

β	Thermal expansion coefficient [K^{-1}]
ϕ	Dimensionless concentration [-]
θ	Dimensionless temperature [-]
σ	Electrical conductivity of the fluid [$S\ m^{-1}$]
μ	Dynamic viscosity of the fluid [$kg\ m^{-2}s^{-1}$]

- ν Kinematic viscosity of the fluid $[m^2 s^{-1}]$
 α Thermal diffusivity of the fluid $[m^2 s^{-1}]$
 ρ_f Density of the fluid $[kg m^{-3}]$
 ρ_p Density of the nanoparticle $[kg m^{-3}]$

REFERENCES

- [1] J. Buongiorno, Convective transport in nanofluids, *ASME J. Heat Transfer*, 128 (2006) 240–250.
- [2] Bouafia, I., Mehdaoui, R., Kadri, S., & Elmir, M. (2021). Conjugate natural convection in a square porous cavity filled with a nanofluid in the presence of two isothermal cylindrical sources. *Journal of Advanced Research in Fluid Mechanics and Thermal Sciences*, 80(1), 147-164.
- [3] Natesan, S., & Arumugam, S. K. (2019). Analysis of double diffusion natural convection in an enclosure filled with alumina water nanofluid using Buongiorno's two phase model. *International Journal of Numerical Methods for Heat & Fluid Flow*, 29(10), 3707-3729.
- [4] Motlagh, S. Y., Taghizadeh, S., & Soltanipour, H. (2016). Natural convection heat transfer in an inclined square enclosure filled with a porous medium saturated by nanofluid using Buongiorno's mathematical model. *Advanced Powder Technology*, 27(6), 2526-2540.
- [5] Yu, Q., Xu, H., & Liao, S. (2018). Analysis of mixed convection flow in an inclined lid-driven enclosure with Buongiorno's nanofluid model. *International Journal of Heat and Mass Transfer*, 126, 221-236.
- [6] Sheremet, M. A., Pop, I., & Rahman, M. M. (2015). Three-dimensional natural convection in a porous enclosure filled with a nanofluid using Buongiorno's mathematical model. *International Journal of Heat and Mass Transfer*, 82, 396-405.
- [7] Oztop, H. F., & Abu-Nada, E. (2008). Numerical study of natural convection in partially heated rectangular enclosures filled with nanofluids. *International Journal of Numerical Methods for Heat & Fluid Flow*, 29(5), 1326-1336.
- [8] Garoosi, F., Garoosi, S., & Hooman, K. (2014). Numerical simulation of natural convection and mixed convection of the nanofluid in a square cavity using Buongiorno model. *Powder Technology*, 268, 279-292.
- [9] Sheremet, M. A., Revnic, C., and Pop, I. (2017). Natural convective heat transfer through two entrapped triangular cavities filled with a nanofluid: Buongiorno's mathematical model. *International Journal of Mechanical Sciences*, 133, 484-494.

- [10] Sheremet, M. A., & Pop, I. (2015). Natural convection in a wavy porous cavity with sinusoidal temperature distributions on both side walls filled with a nanofluid: Buongiorno's mathematical model. *ASME Journal of Heat Transfer*, 137(7), 072601.
- [11] Cimpean, D. S., & Pop, I. (2019). Free convection in an inclined cavity filled with a nanofluid and with sinusoidal temperature on the walls: Buongiorno's mathematical model. *International Journal of Numerical Methods for Heat & Fluid Flow*, 29(12), 4549-4568.
- [12] Sivaraj, R. and Banerjee, S. (2022). Transport phenomena of nanofluids in cavities: current trends and applications. *The European Physical Journal- Special Topics*, 231(13-14), 2487-2490. <https://doi.org/10.1140/epjs/s11734-022-00635-1>
- [13] Sheremet, M. and Pop, I. (2015). Free convection in a triangular cavity filled with a porous medium saturated by a nanofluid. *International Journal of Numerical Methods for Heat & Fluid Flow*, 25(5), 1138-1161. <https://doi.org/10.1108/hff-06-2014-0181>
- [14] Alsabery, A., Chamkha, A., Saleh, H., & Hashim, I. (2017). Natural convection flow of a nanofluid in an inclined square enclosure partially filled with a porous medium. *Scientific Reports*, 7(1). <https://doi.org/10.1038/s41598-017-02241-x>
- [15] Hussein, A. and Mustafa, A. (2017). Natural convection in a parabolic enclosure with an internal vertical heat source filled with cu–water nanofluid. *Heat Transfer-Asian Research*, 47(2), 320-336. <https://doi.org/10.1002/htj.21305>
- [16] Salari, M., Mohammadtabar, A., & Mohammadtabar, M. (2017). Numerical investigation of the effects of geometric parameters of heaters on mixed convection in a lid-driven cavity filled with different nanofluids. *Heat Transfer-Asian Research*, 47(1), 3-26. <https://doi.org/10.1002/htj.21287>
- [17] Ghalambaz, M., Sheremet, M., & Pop, I. (2015). Free convection in a parallelogrammic porous cavity filled with a nanofluid using Tiwari and Das' nanofluid model. *Plos One*, 10(5), e0126486. <https://doi.org/10.1371/journal.pone.0126486>
- [18] Yasuri, A. and Soleimani, E. (2021). An experimental study on the simultaneous effect of nanofluid and tube insert on the thermal performance of an automobile cooling system. *Journal of Applied Fluid Mechanics*, 14(5). <https://doi.org/10.47176/jafm.14.05.32421>
- [19] Cheng, H., Zhou, Y., Feng, Y., Geng, W., Liu, Q., Guo, W., ... & Jiang, L. (2017). Electrokinetic energy conversion in self-assembled 2d nanofluidic channels with janus nanobuilding blocks. *Advanced Materials*, 29(23). <https://doi.org/10.1002/adma.201700177>
- [20] Le, T., Shimizu, H., & Morikawa, K. (2020). Advances in label-free detections for nanofluidic analytical devices. *Micromachines*, 11(10), 885. <https://doi.org/10.3390/mi11100885>

- [21] M. Khani et al., Novel α -alumina@CuO-Fe₂O₃nanofluid for potential application in PEM fuel cell cooling systems: Towards neutralizing the increase of electrical conductivity, *Thermochimica Acta*, 695 (2021) 178818.
- [22] C. Kong, W. Qian, C. Zheng, W. Fei, Enhancing 5 V capacitor performance by adding single walled carbon nanotubes into an ionic liquid electrolyte, *J. Mater. Chem. A*, 3 (2015), pp. 15858-15862.
- [23] A.P. Nagvenkar, L. Shani, I. Felner, I. Perelshtein, A. Gedanken, Y. Yeshurun, Surfactant effect on the thermal and electrical behaviors of sonochemically synthesized Fe and Fe–PVP nanofluids and insight into the magnetism of their in situ oxidized α -Fe₂O₃ analogues, *J. Phys. Chem. C*, 122 (2018), pp. 20755-20762.
- [24] I. Zakaria, W. Azmi, W. Mohamed, R. Mamat, G. Najafi, Experimental investigation of thermal conductivity and electrical conductivity of Al₂O₃ nanofluid in water-ethylene glycol mixture for proton exchange membrane fuel cell application, *Int. Commun. Heat Mass Transf.*, 61 (2015), pp. 61-68.
- [25] S. Khalid, I. Zakaria, W. Azmi, W. Mohamed, Thermal–electrical–hydraulic properties of Al₂O₃–SiO₂ hybrid nanofluids for advanced PEM fuel cell thermal management, *J. Therm. Anal. Calorim.* (2020), pp. 1-13.
- [26] L. Shen, H. Wang, M. Dong, Z. Ma, H. Wang, Solvothermal synthesis and electrical conductivity model for the zinc oxide-insulated oil nanofluid, *Phys. Lett. A*, 376 (2012), pp. 1053-1057.
- [27] S. Bagheli, H.K. Fadafan, R.L. Orimi, M. Ghaemi, Synthesis and experimental investigation of the electrical conductivity of water-based magnetite nanofluids, *Powder Technol.*, 274 (2015), pp. 426-430
- [28] Hussain S, Aly A, Öztop H. Magneto-bioconvection flow of hybrid nanofluid in the presence of oxytactic bacteria in a lid-driven cavity with a streamlined obstacle. *Int Comm. Heat Mass Transfer*. 2022, 134,106029.
- [29] Z. He *et al.*, Electricity generation from artificial wastewater using an upflow microbial fuel cell, *Environ. Sci. Technol.* 2005, 39, 14, 5262–5267.
- [30] Ramdayal Yadav, Akshay Subhash, Nikhil Chemmenchery, Balasubramanian Kandasubramanian. Graphene and graphene oxide for fuel cell technology. *Industrial & Engineering Chemistry Research*, 2018, 57 (29), 9333-9350.
- [31] Jiliang Ci, Chun Cao, Shigenori Kuga, Jianquan Shen, Min Wu, and Yong Huang. Improved performance of microbial fuel cell using esterified corncob cellulose

nanofibers to fabricate air-cathode gas diffusion layer. *ACS Sustainable Chemistry & Engineering* 2017, 5 (11), 9614-9618.

[32] Jeffrey J. Fornero, Miriam Rosenbaum, Michael A. Cotta and LARGUS T. Angenent, Carbon Dioxide Addition to microbial fuel cell cathodes maintains sustainable catholyte pH and improves anolyte pH, alkalinity and conductivity. *Environmental Science & Technology*, 2008, 42 (22), 8578-8584.

[33] N.S. Rathore, N.L. Panwar, Fuel Cell and MHD Technology, in *Fundamentals of Renewable Energy*, 1st Edition, CRC Press, Florida, USA (2021).

[34] N. Xiros, Mathematical Magnetohydrodynamics, *Synthesis Lectures on Mechanical Engineering*, Springer, USA (2018).

[35] O. Anwar Bég, S.K. Ghosh and T. A. Bég, *Applied Magneto-Fluid Dynamics: Modelling and Computation*, 463 pages, Lambert Academic Publishing, Germany, ISBN 978-3-8465-0865-7 August (2011).

[36] P. Barnoon, D. Toghraie, F. Eslami, B. Mehmandoust, Entropy generation analysis of different nanofluid flows in the space between two concentric horizontal pipes in the presence of magnetic field: single-phase and two-phase. *Comput. Math. Appl.* **77**(3), 662–692 (2019).

[37] J. C. Umavathi, K. Vajravelu, O. Anwar Bég and Umar F. Khan, Unsteady squeezing flow of a magnetized dissipative non-Newtonian nanofluid with radiative heat transfer and Fourier-type boundary conditions: numerical study, *Archive of Applied Mechanics* (2022). (17 pages) <https://doi.org/10.1007/s00419-022-02211-4>

[38] M. Amini. A.S.A. Ramazani, S.A. Haddadi, A. Kheradmand. Mechanical, rheological and oxygen barrier properties of ethylene vinyl acetate/diamond nanocomposites for packaging applications. *Diam. Relat. Mater.* 99, 107523 (2019).

[39] M. Kumar, G. J. Reddy, N. N. Kumar and O. Anwar Bég, Computational study of unsteady couple stress magnetic nanofluid flow from a stretching sheet with Ohmic dissipation, *Proc. IMechE-Part N: J Nanoengineering, Nanomaterials and Nano-systems* (2019). (15 pages) DOI: 10.1177/2397791419843730.

[40] Ashwini Hiremath, G. Janardhana Reddy, HussainBasha, N. S. V. Narayanan and O. Anwar Bég, Magnetized supercritical third grade nanofluid flow from a vertical cylinder using a Crank-Nicolson implicit scheme, *Waves in Random and Complex Media* (2022). DOI: 10.1080/17455030.2022.2103207 (32 pages)

[41] M. G. Reddy, K. B. Swetha Latha, D. Tripathi, O. Anwar Bég, S. Kuharat and Martin L. Burby, Ternary Cobalt ferrite (CoFeO₄)-Silver (Ag)-Titanium dioxide (TiO₂) hybrid nanofluid hydromagnetic non-linear radiative-convective flow from a rotating disk with viscous

dissipation, non-Darcy and non-Fourier effects: Swirl coating simulation, *Numerical Heat Transfer- A: Applications* (2023). doi.org/10.1080/10407782.2023.2299295 (28 pages)

[42] Padmaja K, B Rushi Kumar, O. Anwar Bég and T. A. Bég, Mathematical modelling of Cu – H₂O magnetic nanofluid flow with higher order chemical reaction and cross diffusion from a rotating vertical cone adjacent to a porous medium: application to magnetic nanocoatings, *J. Multiscale Modelling (World Scientific)* (2023) 2350006 (21 pages) DOI: 10.1142/S1756973723500063.

[43] J. Philip, Magnetic nanofluids (Ferrofluids): Recent advances, applications, challenges, and future directions, *Advances in Colloid and Interface Science*, 311 (2023) 102810.

[44] Nepal Chandra Roy, MHD natural convection of a hybrid nanofluid in an enclosure with multiple heat sources, *Alexandria Engineering Journal*, 61 (2), 1679-1694 (2022).

[45] W. Al-Kouz, A. Abderrahmane, M. Shamshuddin, O. Younis, S. Mohammed, O. Anwar Bég, D. Toghraie, Heat transfer and entropy generation analysis of water-Fe₃O₄/CNT hybrid magnetic nanofluid flow in a trapezoidal wavy enclosure containing porous media with the Galerkin finite element method, *European Physical Journal Plus* (2021). 136:1184 <https://doi.org/10.1140/epjp/s13360-021-02192-3> (23 pages)

[46] F.M. Azizul *et al.*, MHD mixed convection and heat lines approach of nanofluids in rectangular wavy enclosures with multiple solid fins, *Scientific Reports*, 13, Article number: 9660 (2023).

[47] A. Sumithra, R. Sivaraj, V. R. Prasad, O. Anwar Bég, Ho-Hon Leung, F. Kamalov, S.Kuharat and B.R. Kumar, Computation of inclined magnetic field, thermophoresis and Brownian motion effects on mixed convective electroconductive nanofluid flow in a rectangular porous enclosure with adiabatic walls and hot slits, *International Journal of Modern Physics B* (2024) 2450398 (30 pages) DOI: 10.1142/S0217979224503983 (30 pages).

[48] K. Thirumalaisamy, R. Sivaraj, V. R. Prasad, O. Anwar Bég, H-H. Leung, F. Kamalov and K. Vajravelu, Comparative heat transfer analysis of γ -Al₂O₃ and γ -Al₂O₃-C₂H₆O₂ electroconductive nanofluids in a saturated porous square cavity with Joule dissipation and heat source/sink effects, *Physics of Fluids*, 34, 072001 (2022); (21 pages) <https://doi.org/10.1063/5.0095334>

[49] Venkatadri, K., Bég, O. Anwar & Kuharat, S. (2022). Magneto-convective flow through a porous enclosure with Hall current and thermal radiation effects: numerical study. *The European Physical Journal - Special Topics*, 1-14.

- [50] Venkatadri, K. (2023). Visualization of thermo-magnetic natural convective heat flow in a square enclosure partially filled with a porous medium using Bejan heat lines and Hooman energy flux vectors: Hybrid fuel cell simulation. *Geoenergy Science and Engineering*, 224, 211591.
- [51] O. Anwar Bég, Nonlinear multi-physical laminar nanofluid bioconvection flows: Models and computation, A. Sohail, Z. Li (Eds.): *Computational Approaches in Biomedical Nano-Engineering*, Wiley, Chapter 5, pp. 113-145 (2018). ISBN: 3527344721, 9783527344727.
- [52] Venkatadri, K. (2022). Radiative magneto-thermo-gravitational flow in a porous square cavity with viscous heating and Hall current effects: A numerical study of ψ - v scheme. *Heat Transfer*. <https://doi.org/10.1002/htj.22619>
- [53] Venkatadri, K., Bég, O. A., Rajarajeswari, P., & Prasad, V. R. (2020). Numerical simulation of thermal radiation influence on natural convection in a trapezoidal enclosure: heat flow visualization through energy flux vectors. *International Journal of Mechanical Sciences*, 171, 105391.
- [54] Bég, O. A., Venkatadri, K., Prasad, V. R., Beg, T. A., Kadir, A., & Leonard, H. J. (2020). Numerical simulation of hydromagnetic Marangoni convection flow in a Darcian porous semiconductor melt enclosure with buoyancy and heat generation effects. *Materials Science and Engineering: B*, 261, 114722.
- [55] D. de Vahl Davis, Natural Convection of air in a square cavity: a benchmark solution, *Int. J. Numer. Meth. Fluids*, vol. 3, pp. 249 - 264, 1983.
- [56] M. T. Manzari, An explicit finite element algorithm for convective heat transfer problems, *Int. J. Numer. Meth. Heat Fluid Flow*, vol. 9, pp. 860 - 877, 1999.
- [57] D. C. Wan, B. S. V. Patnaik, and G. W. Wei, A new benchmark quality solution for the buoyancy-driven cavity by discrete singular convolution, *Numerical Heat Transfer, Part B*, 40: 199 - 228, 2001.
- [58] K. Ali *et al.*, Molecular interaction and magnetic dipole effects on fully developed nanofluid flowing via a vertical duct applying finite volume methodology, *Symmetry*, 2022, 14(10), 2007; <https://doi.org/10.3390/sym14102007>.
- [59] R. Bhargava, S. Sharma, P. Bhargava, O. Anwar Bég and A. Kadir, Finite element simulation of nonlinear convective heat and mass transfer in a micropolar fluid-filled enclosure with Rayleigh number effects, *Int. J. Applied Computational Mathematics*, 3 (2), 1347–1379 (2017).
- [60] S. Kuharat, O. Anwar Bég, Ali Kadir and B. Vasu, Computation of metallic nanofluid natural convection in a two-dimensional solar enclosure with radiative heat transfer, aspect

ratio and volume fraction effects, *Arabian J. Science and Engineering* (2020). (19 pages).
doi.org/10.1007/s13369-020-04678-1

[61] Sireetorn Kuharat, O. Anwar Bég, Ali Kadir, B. Vasu, Tasveer A. Bég and W.S. Jouri, Computation of gold-water nanofluid natural convection in a three-dimensional tilted prismatic solar enclosure with aspect ratio and volume fraction effects, *Nanoscience and Technology- An International Journal*, 11(2):141–167 (2020).